Connectome of a human foveal retina

Yeon Jin Kim[1], Orin Packer[1], Thomas Macrina[2], Andreas Pollreisz[3], Christine A. Curcio[4], Kisuk Lee[2], Nico Kemnitz[2], Dodam Ih[2], Tri Nguyen[2], Ran Lu[2], Sergiy Popovych[2], Akhilesh Halageri[2], J. Alexander Bae[2], Joe Strout[2], Stephan Gerhard[5], Robert G. Smith[6], Paul R. Martin[7], Ulrike Grünert[7], Dennis M. Dacey[1,8,*]

[1]Department of Neurobiology & Biophysics, University of Washington, Seattle, WA, 98195
[2]Zetta AI LLC, Sherrill, NY, USA
[3]Department of Ophthalmology, Medical University of Vienna, Vienna, Austria
[4]Department of Ophthalmology and Vision Sciences, University of Alabama at Birmingham, Alabama 35294
[5]Aware LLC, Rappenstrasse 19, 8307 Effretikon, Switzerland
[6]Department of Neuroscience, University of Pennsylvania, Philadelphia, PA 19104
[7]The University of Sydney, Save Sight Institute and Discipline of Ophthalmology, Faculty of Medicine and Health, Sydney, NSW, 2000, Australia
[8]Washington National Primate Research Center, Seattle, WA 98195

***Corresponding author**: Dennis M. Dacey,
Email: dmd@uw.edu

Author Contributions: Y.J.K. and D.M.D. conceived the project. Y.J.K. and D.M.D. generated the ground truth for segmentation and synapses, performed proofreading and created annotations. R.G.S constructed and ran the computational models. Y.J.K. and D.M.D. analyzed the data and generated figures. Y.J.K., D.M.D., P.R.M., and U.G., wrote the paper and consulted on cell type annotations and figure development. C.A.C. and R.G.S., edited the paper. A.P. acquired human tissue. D.M.D., Y.J.K., C.A.C. and A.P. acquired funding. Zetta AI performed EM data alignment, segmentation, synapse detection and cone-cone contactome detection and ingested all data into the CAVE infrastructure for proofreading. S.G. developed 3D visualizations and analysis tools at NeuroMaps.app.

Competing Interest Statement: The authors declare no conflict of interests.

Classifications: Biological Sciences, Neuroscience

Keywords: Foveal retina, Neural Circuitry, Human vision, Color Vision, Connectomics

This file includes:
Main Text (Main text pages: 20, Total pages: 62)
Figures 1 to 10

Abstract

The fovea is a unique specialization of the primate retina and is a promising site for obtaining the first complete connectome of a human central nervous system (CNS) structure. Within the fovea, neural cells and circuits have been miniaturized and compressed during evolution to sample the visual image at highest spatial resolution and begin the neural processing that serves human form, color, and motion perception. Here we present a comprehensive analysis of a sample of human foveal retina using deep learning-based segmentation to reconstruct all cells and synaptic connections at nanoscale resolution. We classified ~3,000 cells into 51 distinct morphological types based on their structural features and connectivity patterns. Our observations reveal novel synaptic pathways absent in non-human primates, suggesting specialized circuits contribute uniquely to human trichromatic color vision. A biophysical model of the distinct connectomes made by gap junctions (electrical synapses) between short- (S) and medium-long- (ML) wavelength-sensitive cone photoreceptors, suggests chromatic interactions between S and ML cones prior to the first chemical synapse. Segmentation of retinal ganglion cells (RGCs) suggests the presence of only 11 visual pathways, with 5 high-density RGC pathways accounting for over 95% of foveal output to the brain: a dramatic contrast to the 40+ ganglion cell types recognized in mouse retina. Our connectomic analysis reveals distinctive features of human neural circuitry and demonstrates how AI-based computational approaches can advance understanding of human brain structure and function.

Significant statement

Vision begins in the retina, an accessible outpost of the brain located at the back of the eye. When we directly view an object, we use the fovea—a tiny region containing over 50 distinct, densely packed neuron types. How these diverse cells interconnect through synapses to transmit visual information has been difficult to determine. Here, we used artificial intelligence-based computational methods to create a complete wiring diagram—a connectome—mapping every neuron and synapse in a sample of human fovea. This connectomic resource will be freely available to researchers worldwide. Discoveries so far include synaptic circuits linked to human color vision, demonstrating how connectomics can reveal what makes the human nervous system unique.

Introduction

The vertebrate retina is an accessible central nervous system (CNS) outpost where the visual process begins. It has long been appreciated for its great complexity(1) and for linking neural structure to visual function(2-4). The retina was an early focus of synaptic-level connectomic reconstruction(5-10), and more recently, retinal cell populations have been linked to their molecular profiles(11-14) and the genetics of human disease(13, 15). Yet even for this intensively studied neural system, we lack a full wiring diagram that could explain how vision—one of our most fundamental senses—is initiated.

The recent achievement of a complete connectome of the brain of the fruit fly, *Drosophila melanogaster*(16, 17), and application of connectomic methods to mm-scale volumes of mouse and human neocortex(18-21), have made the connectome of a larger mammalian brain a conceivable goal(18, 19, 22, 23). In the present study, we take advantage of the distinctive neural architecture of the foveal retina to provide a first-draft connectome of this critical locus in the human CNS.

The fovea is a specialized central region in the retina of humans and other diurnal primates where neural circuits are spatially compressed to facilitate high-resolution form, color and motion perception. At barely 1 mm wide, the fovea encodes only a few degrees of visual space, but its representation is magnified 100-fold across the surface of primary visual cortex(24-28). Accordingly, the fovea is essential for normal vision, and failure of foveal function is a hallmark of devastating blinding retinal diseases. Understanding the fundamental circuit architecture underlying foveal function therefore represents a critical goal.

From a signal-processing viewpoint, the fovea is an input-to-output sensory structure, where light transduction by photoreceptors is processed by diverse neural cell types across two narrow cell and synaptic layers. Here we provide a catalog of human foveal cells and their synaptic assignments to distinct functional circuits. We use this dataset to directly address the long-standing question of the number and identity of visual pathways that link the fovea to the brain. We define only 11 visual pathways, with five accounting for over 95% of foveal output to the human brain, a striking reduction compared to non-primate mammals(29-31) and non-human primates(32, 33). In addition, we observed

94 unexpected differences in synaptic connections compared to non-human primates and provide evidence

95 that neural coding for trichromatic color vision begins with circuitry that is uniquely human.

96

97

Results

Acquisition of the foveal volume. Our goal was to obtain complete retinal circuitry near the peak of cone density (peak of visual acuity)(34, 35). This is a difficult task because foveal cones feed inner retinal circuits via very long axons (Henle fibers, Fig. 1A-1C)(36). Our data sample was therefore centered at 500 µm retinal eccentricity, where cone axon length averages 300-400 µm(37, 38); this location corresponds to cones located ~100-200 µm from the center of the foveal pit (~0.5-1 deg). We cut 3028 vertical sections at 50 nm thickness through a depth of ~150 µm and imaged an area 180 µm tall x 180 µm wide at 5 nm resolution (voxel size, 5 x 5 x 50 nm^3), extending from the Henle fiber layer (outer retina) to the nerve fiber layer (inner retina) (Fig. 1D). Deep learning-based methods (convolutional neural networks)(39, 40) were used to align the images, detect membrane boundaries, segment neurons, glia, blood vessels, conventional (inhibitory) and ribbon (excitatory) synapses, and predict synaptic relationships in the outer and inner synaptic layers (Fig. 1D-1K; see Methods for procedures). We named this volume HFseg1 (Human Fovea, segmented 1). All annotated cell types and the draft catalog of synaptic connections are openly available for exploration using search tools at https://neuromaps.app/datasets (see *SI Appendix*, Table 3), which utilizes the Neuroglancer browser and CAVE infrastructure. In addition, we created a second site, accessed via NeuroMaps, that facilitates proofreading of cells and synapses by the user community.

Cell populations

To derive and understand any connectome, the identity and layout of all cell types must first be clearly understood. Here, we took advantage of the detailed anatomical picture of foveal cell types(41, 42) that has been linked to transcriptomically defined cell clusters in human and non-human primate retina(12, 13, 43). Moreover, for many cell populations the presence of orderly spatial arrays could be used to estimate relative density. We were therefore able to use the original segmentation followed by proofreading of cell morphology (~40,000 edits to date) to annotate and classify all cells and to assess

123 the quality of synapse prediction (Fig. 1F-1G; see *SI Appendix*, Table 1A, 3008 total cells with cell
124 bodies within the volume; ~304,800 total synapses, including those related to processes extending into
125 or through the volume but not linked to cell bodies).

126 In brief, HFseg1 contained 313 cone (pedicles) and 24 rod (spherules) synaptic terminals (rod: cone =
127 0.07, *SI Appendix*, Table 1C, 1D). 17 cone pedicles were identified as short wavelength-sensitive (S)
128 cones (Fig. 2A)(44). The remaining 296 cones comprised long (L) and medium (M) wavelength-sensitive
129 cones, here referred to collectively as LM cones. Postsynaptic to cones, we annotated 268 horizontal
130 cells and 912 bipolar cells (*SI Appendix*, Table 1E, 1F). It was possible to distinguish the H1 and H2
131 horizontal cell types (Fig. 3) and most of the classically recognized bipolar cell types (Fig. 4) by
132 distinctive morphology and connectivity. Some exceptions will be considered further below.

133 We annotated 293 amacrine cells, including 40 cells displaced to the ganglion cell layer (Fig. 5; *SI*
134 *Appendix*, Table 1G; *SI Appendix*, Fig. S8), first dividing cells by dendritic field diameter into small
135 (diameter < 100 μm; n = 189), and large-field (diameter > 100 μm) groups (n = 104). We divided these
136 groups in turn into 19 types (6 small-field and 13 large-field; *SI Appendix*, Table 1G) based on
137 morphology, stratification, mosaic interactions and nuclear morphology (*SI Appendix*, Figs. S3, S6, S8).
138 Figure 5 provides a partial view of this dataset by highlighting four cell types (see also *SI Appendix*,
139 Table 3); two additional amacrine populations are illustrated in *SI Appendix*, Fig. S8 and others can be
140 viewed at the NeuroMaps site.

141 We annotated 599 ganglion cells (Fig. 6; *SI Appendix*, Table 1H). As expected, the classically
142 recognized midget GCs constitute the great majority (536 cells, ~90%)(13, 45); these cells were readily
143 divided into outer-OFF stratifying (n = 280 cells) and inner-ON stratifying (n = 256) types (Fig. 6A, 6E). A
144 second well-defined cell group, the parasol cells (26 cells, 13 inner-ON cells and 13 outer-OFF cells,
145 ~4% of total GCs), was also easily distinguished (Fig. 6B, 6F). Small bistratified GCs(46), found to show
146 blue-yellow color opponency in macaque retina(47, 48) were distinguished by their broad dendritic
147 ramification (12 cells, ~2% of total GCs; Fig. 6C, 6G) and extensive synaptic input from blue cone

148 bipolar cells (BB cells)(49). Together, the midget, parasol and small bistratified cells accounted for
149 95.8% of the ganglion cells in HFseg1 (*SI Appendix*, Table 1H). The remaining 25 ganglion cells showed
150 relatively large dendritic fields (Figs. 6D, 6H–6N) and were divided into 5 provisional groups comprising
151 6 types (*SI Appendix*, Table 1H; Supporting Information Text) pending a more detailed analysis of their
152 synaptic connections, giving a total of 11 ganglion cell populations in this volume–this number is very
153 close to the 12 populations identified for central human retina by molecular profiling(13).

154 Finally, glial cells were readily distinguished from all neurons by their distinctive ultrastructure (*SI*
155 *Appendix*, Figs. S3A, S3B, S3C, S3F). The Müller cells (555 cells, Fig.1F, 1G; *SI Appendix*, Table 1B)
156 were distinguished as radial glia with cell bodies in the inner nuclear layer (*SI Appendix*, Fig. S1A). A
157 second, morphologically distinct population of glial cells in the GCL was closely associated with
158 superficial blood vessels (*SI Appendix*, Figs. S1B, S3B) and identified as astrocytes(50) (32 cells, *SI*
159 *Appendix*, Table 1B). We also identified 15 microglial cells (*SI Appendix*, Table 1B) with cell bodies in
160 the IPL or GCL (*SI Appendix*, Figs. S1A, S3A). The density of microglial cells was low, consistent with
161 previous measurements in the macaque monkey foveal retina(51, 52). In the current volume, we have
162 not yet attempted to characterize blood vessel and associated pericytes, though these cellular elements
163 are also segmented and are available to annotate and further characterize. More detailed information on
164 cell type identification is provided in the supporting information (Supporting Information Text on Cell type
165 identification).

166

167 **Synapse detection**

168 To assess the accuracy of ribbon segmentation and synapse prediction (Fig. 1H-1K), we compared
169 deep-learning-predicted synaptic assignments to manual (ground truth) assignments. We focused on the
170 cone-to-midget bipolar cell synapse in the OPL and the midget bipolar cell synapses to amacrine and

171 ganglion cells in the IPL. For ground truth, we manually annotated all midget pathway synaptic
172 connections for three LM cones (cones 21, 22, and 58; *SI Appendix*, Fig. S9; *SI Appendix*, Table 2A-2C).

173 Figure 7 shows the predicted outgoing synapses for a pair of midget bipolar cell axon terminals. We
174 calculated precision (true synapses / [true synapses + false positives]; the accuracy of positive
175 predictions) and sensitivity (true synapses / [true synapses + false negatives]; the proportion of true
176 synapses identified) for ribbons and their synapses. The segmentation of ribbons showed high precision
177 and sensitivity near 100% (precision: 93.5% ± 2.7%; sensitivity: 99.7% ± 0.8%, n = 6 midget bipolar
178 cells, 370 total ribbons; Fig. 7B inset). Postsynaptic partner assignment for these ribbons was also
179 excellent (precision: 89.0% ± 5.4%; sensitivity: 93.7% ± 4.6%, n = 6 midget bipolar cells, 637 total
180 synapses; Fig. 7B inset). These values demonstrate the high accuracy of convolutional nets for
181 predicting and segmenting ribbon synapses.

182 In contrast to the ribbon synapses made in the IPL, ribbon synapses made by the cone pedicle in the
183 OPL are extremely complex(53, 54) (Fig. 1H, 1I). Postsynaptic processes can either invaginate into the
184 face of the pedicle or occupy a basal position at the cone pedicle up to ~800 nm from the sites of
185 transmitter release(54, 55). We mapped all cone-to-bipolar synapses at the dendritic tips for a sample of
186 six midget bipolar cells. We found high precision and sensitivity for ribbon detection (n = 51 ribbons)
187 (precision: 92.3% ± 6.7%; sensitivity: 100%, n = 3 LM cones, *SI Appendix*, Fig. S2A-S2C) and for the
188 postsynaptic processes (n = 153) deriving from the invaginating (IMB) and flat (FMB) midget bipolar cells
189 (precision: 98.7% ± 1.2%; sensitivity: 99.7% ± 0.6%, n = 153 total synaptic connections; see *SI*
190 *Appendix*, Fig. S2C right). Diffuse bipolar (DB) cells, which make sparser connections with multiple
191 cones, were also sampled (n = 2, DB4 and DB2; *SI Appendix*, Fig. S2D-S2F), yielding similar precision
192 and sensitivity values.

193 For inhibitory synapses, we focused on the AII amacrine cell (Figs. 5A, 7C, 9; *SI Appendix*, Table 1G)
194 where glycinergic synapses to OFF bipolar cell axon terminals are well established(56-59). We manually
195 mapped all the outgoing synapses made by two neighboring AII amacrine cells and compared our

196 ground truth data to the predicted synaptic assignments (Fig. 7C-7G). The prediction captured well the
197 synaptic output from the outer stratifying lobular appendages of the AII cell to outer-OFF bipolar cells
198 (Fig. 7D-7G). Vesicle clouds were detected with high sensitivity (87.5% ± 0.7%, n = 2 AII cells; false
199 negatives were rare; Fig. 7C inset), but relative to ribbon detection, there were more false positives,
200 thereby reducing precision (76.0% ± 8.5%, n = 2 AII cells). Despite this limitation, the results show that
201 our dataset predicts synaptic connectivity with good sensitivity and precision. However, we implemented
202 methods within the Neuromaps interface to proofread all synapses for accuracy.

203 Having established the accuracy of our connectomic dataset, we examined the cell types and their
204 synaptic connections to identify features that are distinctive in human compared to non-human primates.
205 Below we highlight examples where differences are dramatic and warrant further study.

206

207 **Modeling the connectome: S-LM cone electrical coupling alters spectral tuning.**

208 Cone pedicles contact each other by short extensions (telodendria) or by distinct pedicle-to-pedicle
209 appositions at perforations in the glial sheath surrounding cone synapses (Fig. 2B). These contacts
210 harbor gap junctions, i.e., electrical synapses that mediate a conductance between cones, including L
211 and M cones(60). In non-human primates, L to M cone contacts are abundant, but S to LM contacts are
212 greatly reduced or absent(44, 61). In the macaque, electrical coupling was absent between LM and S
213 cones(60), consistent with a lack of contacts between these cone types(61, 62). The crosstalk between
214 L and M cones serves to reduce noise in the light-evoked response with a small cost to spectral
215 separation(63-65). The lack of gap junctions between LM and S cones has been interpreted as reflecting
216 the need to keep S and LM cone signals separate to build color-coding receptive fields at later stages in
217 color processing(66, 67).

218 Unlike in the macaque, S-LM cone contacts have been reported in human retina(44, 68). We therefore
219 mapped the full cone-cone connectome to determine whether S-LM contacts are a consistent feature of

220 the human fovea. Cone-cone contacts (n = 1141) were characterized by a thick, darkly stained region
221 defining the contact area (see Fig. 2C)(69). We found abundant S-LM cone contacts (n = 17 S cones;
222 5.25 ± 2.11 contacts/S-cone pedicle), indistinguishable from LM-LM cone contacts (n = 296 LM cones;
223 6.89 ± 3.08 contacts/pedicle). We then used this cone-cone connectome dataset to estimate the effect
224 of S-LM coupling on spectral tuning in a simulated cone-cone network, using known parameters for gap
225 junction number and single channel conductance values as follows. We mapped the surface area of the
226 contacts among all cones in the volume (Fig. 2A), using automated methods to generate the
227 "contactome" between cone pedicles. Detected contacts were inspected and filtered by size to remove
228 very small and likely spurious contacts. The surface area of each contact was calculated (n = 1141
229 contacts; mean surface area 0.56 ± 0.31 μm^2). In general, contacts were large and obvious with a
230 relatively thick, darkly stained region defining the contact area (see Fig. 2C), reflecting the presence of
231 large adherens junctions at the contact site(69). We calculated the conductance for each contact based
232 on previously measured densities for gap junctions and the conductance of single gap junction channels
233 (9 gap junctions/μm^2 at 15 pS/junction; see Methods for details). We used a fixed ratio of L to M cones
234 of ~1.7:1, randomly assigned(70), and incorporated the cone-cone coupling given by our contactome
235 (Fig. 8A). Each cone was modeled compartmentally as a soma, Henle fiber-axon, and synaptic terminal
236 (see model parameters in *SI Appendix*, Table 4). Our modeled average coupling conductances were low
237 (LM-LM cone pairs, 133 pS, n = 25 cones; S-LM cone pairs, 166 pS, n = 15) by comparison with
238 conductances measured directly between LM cone pairs in the macaque (> 500 pS) or cone pairs in
239 non-primate mammalian retina (~220-320 pS)(65, 67). Nevertheless, we found that even with this
240 conservative estimate of coupling conductance, the S-cones showed an increased sensitivity to light
241 pulses at longer wavelengths in the model (Fig. 8B). We measured the effect on spectral sensitivity by
242 simulating light responses from L, M, and S cones at 5 nm wavelength intervals across the visible
243 spectrum. The results demonstrate a broad secondary elevation in sensitivity for S cones at longer
244 wavelengths that peaks at ~550 nm (Fig. 8C-8D) in the coupled cone network. These data provide

245 evidence that S-LM cone coupling can directly influence the spectral tuning of the voltage response of S
246 cones and raise the question of how this network feature affects downstream processing.

247

248 **Trichromatic horizontal cells**

249 A second difference in synaptic connectivity that may impact color vision occurs at the synapse between
250 cones and horizontal cells. The horizontal cell network in the outer retina generates lateral negative
251 feedback that underlies the antagonistic receptive field surround of cones, bipolar cells, and ganglion
252 cells(71). In the macaque monkey retina, the horizontal cell-mediated surround is a key element in the
253 circuitry that initiates red-green color vision(72-74). In the peripheral retina of the macaque and
254 marmoset, H1 cells make dense contacts with LM cones but largely or completely avoid contact with S
255 cones, whereas H2 cells show some selectivity for S cones(75-77). While foveal H2 cells in HFseg1
256 maintained a clear preference for synapsing with S cones (Fig. 3B), we found that H1 cells also received
257 a major input from S cones, comparable to H2 cells (H1, 43% ± 16%; H2, 57% ± 16%, n = 10 S cones).
258 By contrast, H2 cells formed less than 2% of the horizontal cell contacts with LM cones (H1, 98.1% ±
259 0.1%; H2, 1.9% ± 0.1%, n = 2 LM cones) (see also *SI Appendix*, Fig. S4). Consequently, human foveal
260 H1 cells are predicted to show a trichromatic receptive field with a small S cone contribution (Fig. 3; *SI*
261 *Appendix*, Fig. S4). Taken together, the S-LM cone coupling and the combined S and LM cone
262 connectivity of H1 horizontal cells provide new connectomic evidence for differences between human
263 and non-human primate circuits that initiate color vision(44).

264

265 **Unexpected cell types and circuits in HFseg1**

266 We also found differences in both bipolar and amacrine cell circuits compared to expectations from the
267 macaque monkey, whereby some bipolar cell types were either greatly reduced or absent. For example,
268 DB-OFF bipolar cells can be divided into 4 morphological types (DB 1, 2, 3a and 3b) in macaque

269 monkey(78, 79) but we were only able to distinguish three populations by mosaic arrangement and
270 stratification in the IPL that we call DB1, 2 and 3 (see Supporting Information Text). Bipolar cell
271 morphologies not previously described in primates were also present. One bipolar group showed
272 amacrine-like morphology (outer-x and inner-x, Fig. 4A, 4B) but contained abundant synaptic ribbons
273 (20 cells, *SI Appendix*, Table 1F; *SI Appendix*, Fig. S6). Similar cells were discovered recently in mouse
274 retina(11, 80) and likely correspond to the OFF-x bipolar cells identified by transcriptomics of human
275 fovea(13). While most of these cells stratified in the outer half of the IPL (outer-x cells, n = 15, *SI*
276 *Appendix*, Fig. S6A-S6B), five cells stratified in the inner half of the IPL (inner-x cells, *SI Appendix*, Fig.
277 S6C-S6G). Another previously undescribed bipolar type showed the characteristic DB cell connection to
278 multiple cones but extended axonal branches in both outer and inner IPL where it provided synaptic
279 output to outer-OFF and inner-ON ganglion cell types (see also *SI Appendix*, Fig. S7C, S7E). We refer
280 to this cell group as DBbroad (18 cells, Fig. 4A; *SI Appendix*, Fig. S7; *SI Appendix*, Table 1F). The
281 HFseg1 volume offers a unique opportunity to further understand these novel bipolar cell populations.

282 For the amacrine cells, the AII type (AC2) was present at the highest density of any amacrine cell
283 population (26%, 75 cells, Figs. 5A, 5B, 7C, 9; *SI Appendix*, Table 1G). This cell type was recognized by
284 its well-established morphology across species(56), including humans(41, 57, 81). A major function of
285 AII cells is to transfer signals from rod bipolar to cone bipolar cells, serving as conduits for rod signals to
286 ganglion cells at scotopic light levels(82). The presence of AII amacrine cells at such a high density in
287 the fovea, where rods are nearly absent, suggests, however, a functional switch to a primary role in
288 photopic spatial vision. Indeed, we observed that AII cells are postsynaptic to all cone bipolar types,
289 including IMB and FMB cells, across the full extent of the dendritic tree (Fig. 9). These data support the
290 general view that AII cells “have a day job”(57) to provide an inhibitory pathway from ON to OFF bipolar
291 cells under photopic conditions(82-84) while at the same time suggesting specialized synaptic
292 alterations for the AII cells in the human fovea in relation to the midget circuit.

293

294 **Visual pathway reduction: the vertical excitatory connectome**

295 Despite its fundamental importance, the number of visual pathways linking the human fovea to the brain
296 is still unknown. Our classification of 11 ganglion cell types suggests that several ganglion cell types
297 observed in the monkey and human retinal periphery are absent from the human fovea. This result also
298 stands in sharp contrast to the retina of the mouse, where ~40 GC types have been distinguished
299 independent of retinal location(29-31). Our classification, however, did not rule out the possibility that
300 some ganglion cell types with somata outside HFseg1 have dendritic trees which penetrate the volume
301 and contribute substantially to the synaptic connections of the inner retina. We therefore took a second
302 approach to identifying the visual pathways in HFseg1 by mapping what we called the "vertical excitatory
303 connectome".

304 We reasoned, as others have(85), that to generate parallel pathways to the brain, each cone
305 photoreceptor must be locally presynaptic to each cone bipolar type (For the S cones there is
306 uncertainty regarding this point, due to their more specialized role in color vision(86, 87)). At the next
307 synaptic step, the combined output of all bipolar cell types should be distributed to all ganglion cell
308 types. In other words, in principle, *all visual pathways should be synaptically linked to the output of any*
309 *given cone*.

310 To test this hypothesis, we annotated the ribbons within five cones (three LM and two S) and their
311 postsynaptic bipolar cells. For each bipolar cell, all synaptic ribbons and their postsynaptic GC partners
312 were then identified (Fig. 10A-10B). Finally, we determined the relative synaptic density from a given
313 cone via its postsynaptic bipolar cells to each identified GC type (see details in *SI Appendix*, Figs. S9
314 and S10; *SI Appendix*, Table 2).

315 We found that bipolar cells that were postsynaptic to the three LM cones provided their output
316 overwhelmingly to midget and parasol ganglion cells (*SI Appendix*, Fig. S9), accounting for 92.1% of the
317 total bipolar synaptic output to ganglion cells (Fig.10C, 10D; *SI Appendix*, Fig. S9; *SI Appendix*, Table

318 2A-2C). The remaining ~7.9% of bipolar synapses were directed to the large-field ganglion cell types
319 (LFGC1-LFGC5, Fig.10C, 10D; *SI Appendix*, Fig. S9; *SI Appendix*, Table 2A-2C). Output to dendritic
320 fragments of unidentified ganglion cells was rare, accounting for only ~0.5% of the total bipolar output to
321 ganglion cells (0.53 ± 0.76%, n = 3 LM cones; *SI Appendix*, Table 2A-2C). These data support the
322 conclusion that, with the possible exception of extremely large-field and low-density melanopsin-
323 expressing ganglion cells, we have accounted for all ganglion cell types present in our foveal sample.

324

325

326 **Discussion**

327 **A human foveal connectome.** Our aim was to provide a draft nanometer-scale connectome in the
328 human CNS. Compared to ongoing studies of a larger volume of human neocortex(18), our foveal
329 volume has the advantage that foveal circuitry is miniaturized and functionally complete – from receptors
330 to ganglion cell outputs. Moreover, all cell types in the HFseg1 volume are identified and can be related
331 to anatomical, physiological, and transcriptomic studies of human and non-human primate retina (*SI*
332 *Appendix*, Table 1).

333

334 **Cell type profiling.** Comparable datasets to HFseg1 exist for primate central retina where cell types
335 were clustered by gene expression profiles(12, 13, 15, 43, 88). The HFseg1 volume permits a
336 comparison of the two approaches and suggests generally good correspondence, though with some
337 unexpected differences. For example, the ratio of H1 to H2 horizontal cell types identified by
338 transcriptomic analysis was shown in the macaque and human central retina to be ~3:1 and 7:1,
339 respectively. By contrast, the H1 to H2 ratio in HFseg1 is much higher (22:1), with H1 cells comprising
340 96% of the horizontal cells at this foveal location. Thus, the trend toward H1 cell dominance in the
341 transcriptomic dataset is evident but more extreme in HFseg1. A similar trend holds for other clearly
342 identified types: for example, midget ganglion cells make up ~90% of the ganglion cell population in our
343 sample and 86% in the transcriptomic dataset; AII amacrine cells make up 26% of the amacrine cells
344 but only 18% of the amacrines identified by transcriptomic analysis. One explanation for these
345 differences may be that our smaller sample represents the cone-enriched foveal center, whereas the
346 larger samples used for transcriptomics encompassed a much larger area (~1.5 mm, central 5 degrees).
347 Cell type-specific density changes are extremely steep across this region, thus, larger spatial samples
348 would average out such changes.

349 Certain cell populations previously recognized were not evident in HFseg1. For example, the recent
350 functional, anatomical, and molecular distinction made between DB3a and DB3b in the macaque

351 monkey(79, 89) and human retina(13, 38) was not apparent in HFseg1. Further, we found evidence for
352 only 19 amacrine cell types, whereas molecular profiling in human retina (including the retinal periphery)
353 has proposed 73 amacrine cell types(15). By comparison, 63 amacrine clusters have been identified in
354 mouse retina(90, 91). These differences suggest that the relationship between cells defined by gene
355 expression and anatomical types may not always be straightforward. A further implication is that the
356 extreme increase in density of the midget circuit, required for high acuity and color vision, gives rise to
357 an attendant density increase in other foveal cell types tightly linked to the midget pathway (e.g., H1
358 horizontal cells).

359

360 **The vertical excitatory connectome.** In the non-human primates, fewer than 20 ganglion cell types
361 have been defined, with transcriptomic and anatomical identification in close agreement(12, 32, 33). In
362 the human fovea, only 12 pathways have been suggested by transcriptomic analysis(13, 15). It was
363 nevertheless striking that in the HFseg1 dataset (*SI Appendix*, Table 1H), ~96% of the ganglion cells
364 comprised just five anatomically distinct pathways: the ON and OFF midget and parasol cells, and the
365 small bistratified cells. When we manually traced the vertical connectome from a single cone to its
366 postsynaptic bipolar and ganglion cells, we found that ~92% of synaptic output targeted these same five
367 pathways (Fig. 10D), confirming their dominance. Thus, a fundamental, defining feature of foveal
368 synaptic organization may be a reduction in the number of visual pathways compared to the peripheral
369 retina.

370 Over 40 distinct ganglion cell populations have been recognized in the mouse retina, with molecular
371 profiling, physiology, and anatomy in agreement(29-31). What explains this dramatic reduction in
372 ganglion cell types from the mouse retina to the primate fovea? The difference suggests that humans
373 and mice have evolved fundamentally different solutions to analyzing the visual scene. Great emphasis
374 has been placed on the behaviorally relevant feature-detection properties of diverse mouse ganglion

375 cell types(92-94). By contrast, in primates, considerable emphasis has been placed on the dual and
376 more general role of the midget pathway in both form and color perception(74, 95, 96).

377 Recent molecular orthotype analysis shows that the midget and parasol ganglion cell types are likely
378 homologous to sustained and transient alpha cell types, respectively, in the mouse(14). What differs
379 dramatically, however, is the extremely large dendritic tree and consequent low spatial density (~2% of
380 the total ganglion cells) of the mouse ortholog of the midget ganglion cell. Thus, the mouse retina
381 sacrifices spatial resolution(97), opting instead for an expansion of feature detectors that mediate
382 visually driven reflexive behaviors—with mice employing feature-detection strategies analogous to
383 those described in classical studies of amphibian vision(98). In primates, the midget circuit represents
384 an evolutionary extreme where the spatial resolution afforded by tightly packed photoreceptors is
385 preserved through private-line connectivity. This high-resolution sampling is behaviorally exploited
386 through active vision strategies. Humans not only explore a visual scene by making saccadic eye
387 movements but also make small fixational eye movements (microsaccades) to extract information at
388 peak resolution(99). These microsaccades are dynamically modulated during highly precise
389 manipulation (e.g., threading a needle)(99-101). Thus, the incessantly mobile fovea and related retinal
390 circuits are designed for inspection, manipulation, interpretation, and understanding of an object—the
391 converse of a feature detector.

392

393 **The foveal connectome and human color vision.**

394 *S cone input to H1 cells.* Most psychophysically based models of human color vision assume the
395 presence of two parallel color-opponent channels: red vs green and blue vs yellow[109]. The red-green
396 pathway shows opposing L vs M cone interaction and has been associated with the circuitry that feeds
397 midget ganglion cells(102). However, the human psychophysically defined red-green pathway includes a
398 small S cone input(103). The locus of this critical signal pathway remains unclear, with recent data from

399 the macaque monkey implicating both the retina[110] and primary visual cortex[111]. The HFseg1
400 connectome shows that H1 horizontal cells, a major source of the surround in the midget circuit[51], likely
401 contribute antagonistic signals from all three cone types (L, M, and S) to the midget pathway. In this
402 scenario, the human foveal midget circuit would derive its center response from either an L or M cone,
403 while the surround would provide cone opponency by non-selectively contacting all three cone types(73,
404 104, 105), with the S cones making a small contribution to the chromatic receptive field, creating L+S vs
405 M or M+S vs L opponency.

406 *S-LM cone coupling.* As a first step in deriving the foveal connectome, we determined the "contactome"
407 among the tightly packed cone synaptic pedicles. Contacts among the cone types harbor gap junctions
408 and thus form electrical synaptic connections between cones(65, 69). We confirmed and extended
409 previous observations suggesting that, in contrast to non-human primates and non-primate mammals,
410 human foveal S cones show extensive telodendritic contacts with neighboring LM cones(44, 68), and
411 these contacts are identical in form to LM-LM cone contacts.

412 A network model of this connectivity showed that, as a previous model suggested(66), mixing S and LM
413 cone signals can alter the action spectrum of the S cone light response, with increased sensitivity at
414 longer wavelengths. This result raises a functional puzzle: the prevailing view is that electrical coupling
415 serves to increase signal relative to noise by reducing the uncorrelated voltage difference (i.e., the noise
416 component) among neighboring cones and thereby increase contrast sensitivity(66). However, any
417 mixing of S and LM cone signals would detract from the separation of cone signals required for color
418 processing, in turn raising the question of why such coupling occurs in human foveal retina, whereas it is
419 absent in both the macaque and marmoset retina(44).

420 The answer may be related, at least in part, to the connectivity of H1 horizontal cells with S cones noted
421 above. Coupling among the S, L, and M cones prior to this connection may serve to preserve the
422 smaller S cone signal within the H1 cell network. This in turn may be critical for the unique requirements
423 of human color vision whereby a small S cone signal contributes critically to the "red-green" chromatic

channel defined psychophysically(103). This hypothesis could be tested by adding the horizontal cell connectome to the current cone-cone network and testing the effects of noise and coupling on the spectral tuning of the H1 cell response and ultimately its contribution to cone opponency modeled in the midget ganglion cell.

Acknowledgements

This work was supported by NIH grants EY-028282 and RF1-MH129260 to D.M.D. and NIH grant P51 OD010425 to the Washington National Primate Research Center and EY01730 to the Vision Research Core at the University of Washington. We thank Sharm Knecht for tissue preparation and managing EM data acquisition.

Author contributions

Y.J.K. and D.M.D. conceived the project. Y.J.K. and D.M.D. generated the ground truth for segmentation and synapses, performed proofreading and created annotations. R.G.S constructed and ran the computational models. Y.J.K. and D.M.D. analyzed the data and generated figures. Y.J.K., D.M.D., P.R.M., and U.G., wrote the paper and consulted on cell type annotations and figure development. C.A.C. and R.G.S., edited the paper. A.P. acquired human tissue. D.M.D., Y.J.K., C.A.C. and A.P. acquired funding. Zetta AI performed EM data alignment, segmentation, synapse detection and cone-cone contactome detection and ingested all data into the CAVE infrastructure for proofreading. S.G. developed visualization and analysis tools at NeuroMaps.app.

Declaration of interests

K.L., N.K., D.I., T.N., R.L., S.P., A.H., J.A.B., J.S. and T.M. declare financial interests in Zetta AI. S.G. is owner of Aware LLC and developed the NeuroMaps.app. The remaining authors declare no competing interests.

448 **Figures and figure legends (10 Figures)**

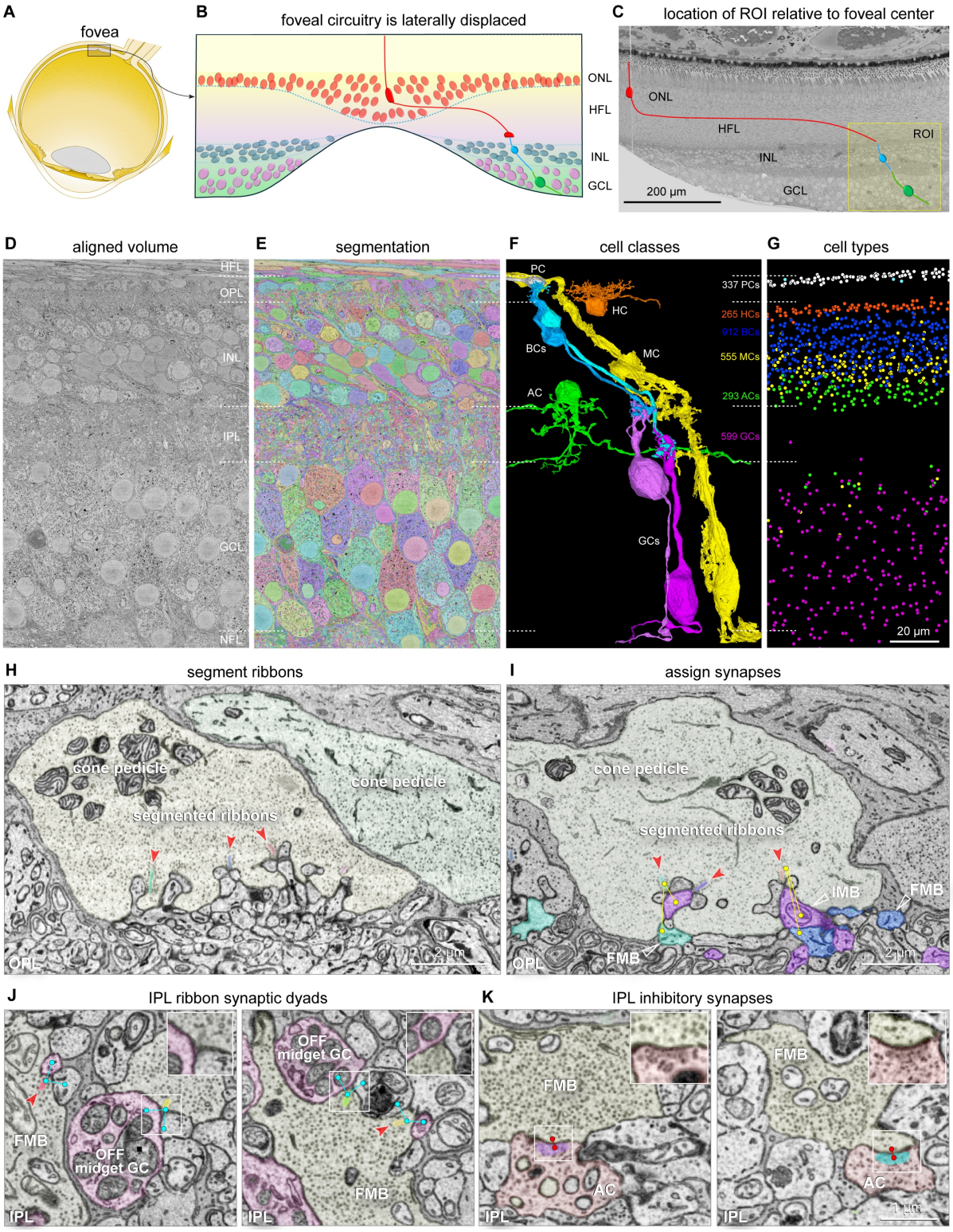

449

450 **Fig. 1. The HFseg1 volume**. **A.** The fovea forms a pit in the retina ~3 mm temporal to the optic disc
451 (within the inset rectangle). **B**. Schematic foveal pit showing cone (red) to bipolar cell (blue) to ganglion
452 cell (green) circuit. ONL (outer nuclear layer), HFL (Henle fiber layer), INL (inner nuclear layer), GCL
453 (ganglion cell layer). **C**. Trimmed retinal block face and ROI (yellow box) in temporal retina 400-500 μm
454 from the foveal center. **D**. Single section from the imaged volume (cropped laterally) to illustrate the
455 retinal layers. HFL, OPL (outer plexiform layer), INL, IPL (inner plexiform layer), GCL, and NFL (nerve
456 fiber layer). **E**. Volume segmented into membrane-bound objects. **F**. Examples of segmented cells:
457 photoreceptor axon terminal (PC, white), horizontal cell (HC, orange), ON and OFF bipolar cells (BC,
458 light and dark blue), Müller glia cell (MC, yellow), amacrine cells (AC, green), ON and OFF ganglion
459 cells (GC, dark and light violet); astrocytes and microglia not shown here. **G**. Numbers and soma
460 locations of the cell types shown in **F**. **H.** Three segmented ribbons (varied colors) at synaptic triads
461 (red arrowheads) in a single cone pedicle. **I.** Synaptic assignments associated with each ribbon (yellow
462 dots and lines). An IMB (inner-ON midget bipolar, violet, white open arrowhead) cell makes an
463 invaginating contact and two FMB cells (outer-OFF midget bipolar, light and dark blue, white open
464 arrowheads) make a basal contact with the cone pedicle. **J.** Examples of ribbon and synapse prediction
465 in the inner plexiform layer (IPL) for an FMB cell axon terminal at two locations (left and right panels).
466 Segmented ribbons (varied colors, red arrowheads) and synaptic predictions (blue dots, lines) are
467 shown. **K.** Inhibitory vesicle cloud segmentation (varied colors) and synaptic prediction (red dots and
468 lines) between an amacrine cell and an FMB axon terminal in the IPL. Insets in **J** and **K** show zoomed
469 view of synapses indicated by white boxes.

470

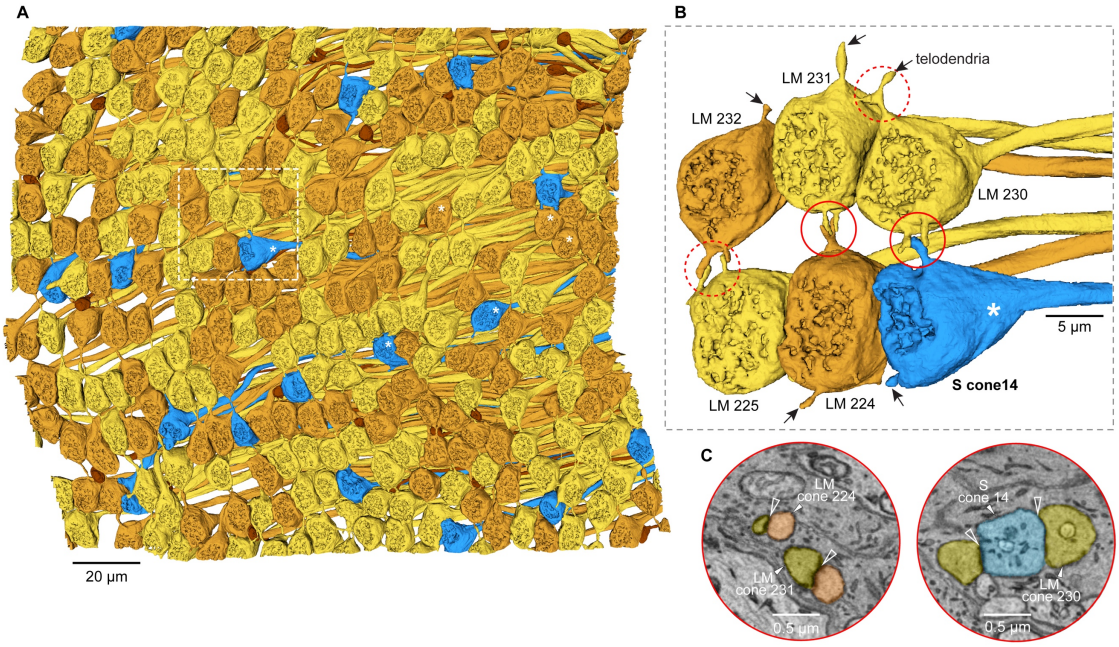

Fig. 2. Photoreceptors. A. Array of photoreceptor axon terminals (cone pedicles, rod spherules) viewed from the synaptic face of the terminals (296 LM cones, gold; 17 S cones, blue; 24 rods, brown) (see *SI Appendix*, Table 1A, 1C, 1D). Five cones marked with white asterisks were used to generate the vertical connectome analysis shown in *SI Appendix*, Figs. S9 and S10 (S cones 54 and 103; LM cones 21, 22, and 58). **B**. Six cone pedicles within the white dotted box in **A**. These pedicles contact each other via telodendria (e.g., arrows) within the circled areas. One pedicle, identified as S cone 14 (white asterisk), contacts neighboring LM cone 230. **C**. EM micrographs showing telodendritic contacts (open white arrowheads) corresponding to the two solid red circled areas in **B**. **Left**: contact between LM cones 231 and 224. **Right**: S cone 14 contact with LM cone 230. Cone-cone contact surface areas were calculated and used in the simulation shown in Fig. 8.

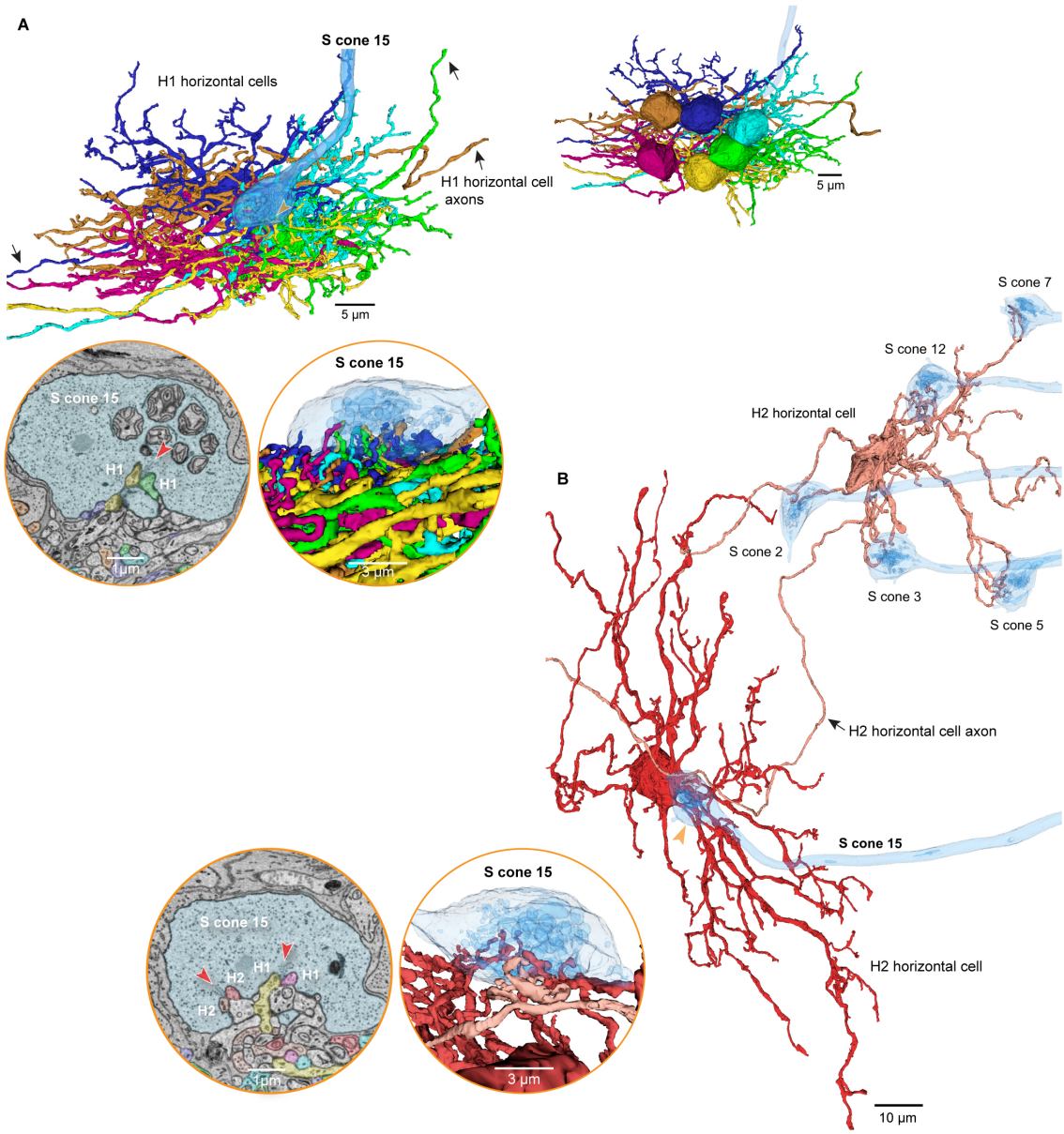

482

483 **Fig. 3. H1 and H2 horizontal cells synapse with S cones. A.** Six overlapping H1 cells are shown
484 (varied colors); each H1 cell forms lateral elements at S cone 15 (blue). Upper right inset shows an
485 inverted view of the cell bodies of the six H1 cells. Lower left inset shows EM view of H1 cell lateral
486 elements at a synaptic invagination of S cone 15 (red arrowhead). Lower right inset shows a 3D view of
487 S cone 15 (partial transparency) contacting multiple H1 cells. H1 cells made 43% ± 16% of the total
488 contacts with S cones (n = 10 S cones). **B**. Two H2 cells (tan and red) contact multiple S cones,
489 including S cone 15. Lower insets show H2 cell lateral elements at S cone 15 in single-layer EM (left)

490 and 3D (right) views (as in **A**). H2 cells made 57% ± 16% of the total contacts with S cones (n = 10 S

491 cones).

492

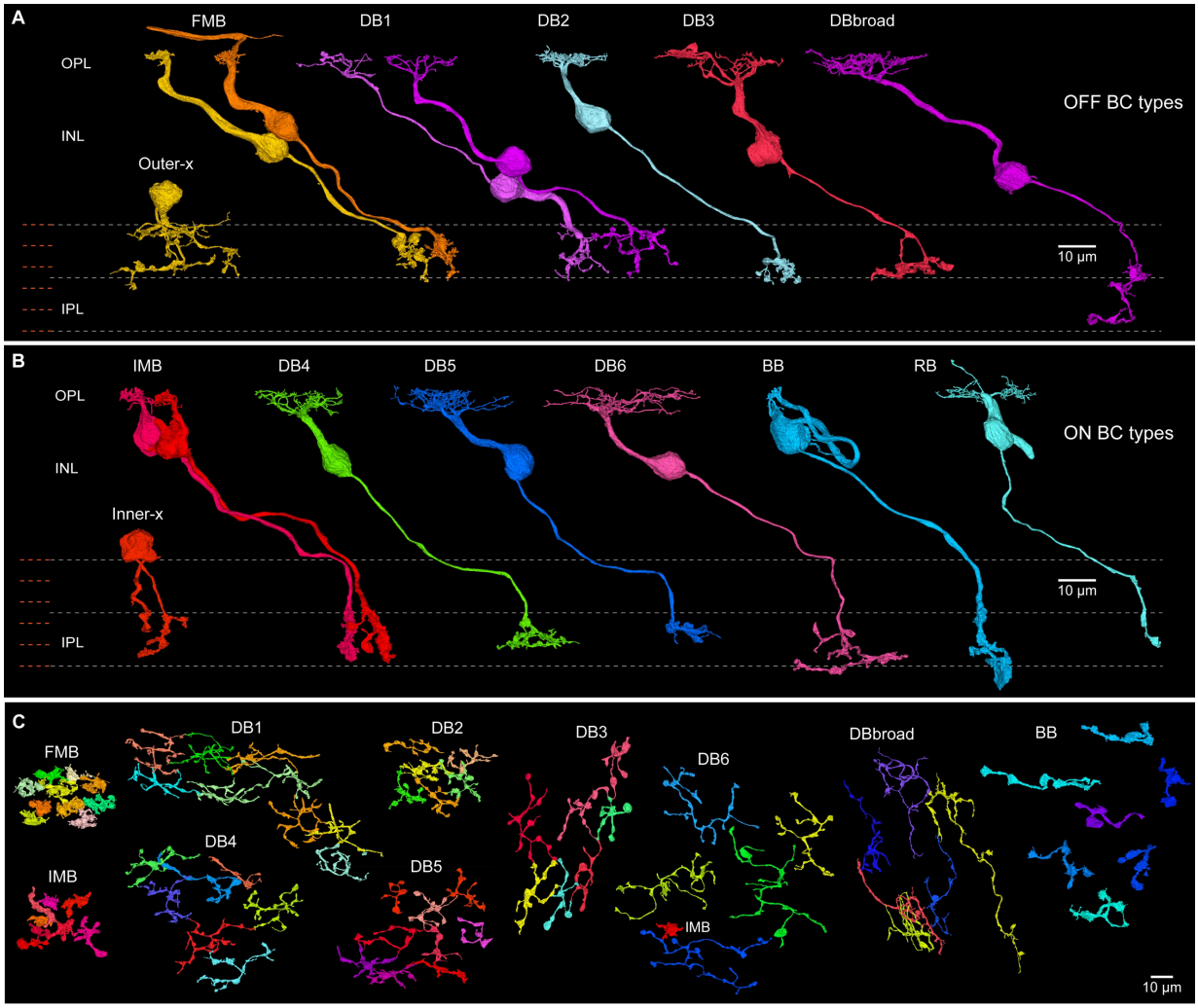

493

494 **Fig. 4. Bipolar cell types. A**. Outer stratifying types: FMB (flat midget bipolar), DB (diffuse bipolar

495 types). Outer-x bipolar cells lack dendrites but make ribbon synapses in the IPL (*SI Appendix*, Fig.

496 S6A). DBbroad cells extend processes across the IPL depth (*SI Appendix*, Fig. S7). **B.** Inner stratifying

497 bipolar types: IMB (invaginating midget bipolar), DB (diffuse bipolar types), BB (blue-cone bipolar), RB

498 (rod bipolar). Inner-x bipolar cells are shown in *SI Appendix*, Fig. S6C. **C**. Horizontal view of spatial

499 mosaics of axon terminals for small groups of neighboring cells of each bipolar type, as labeled.

500

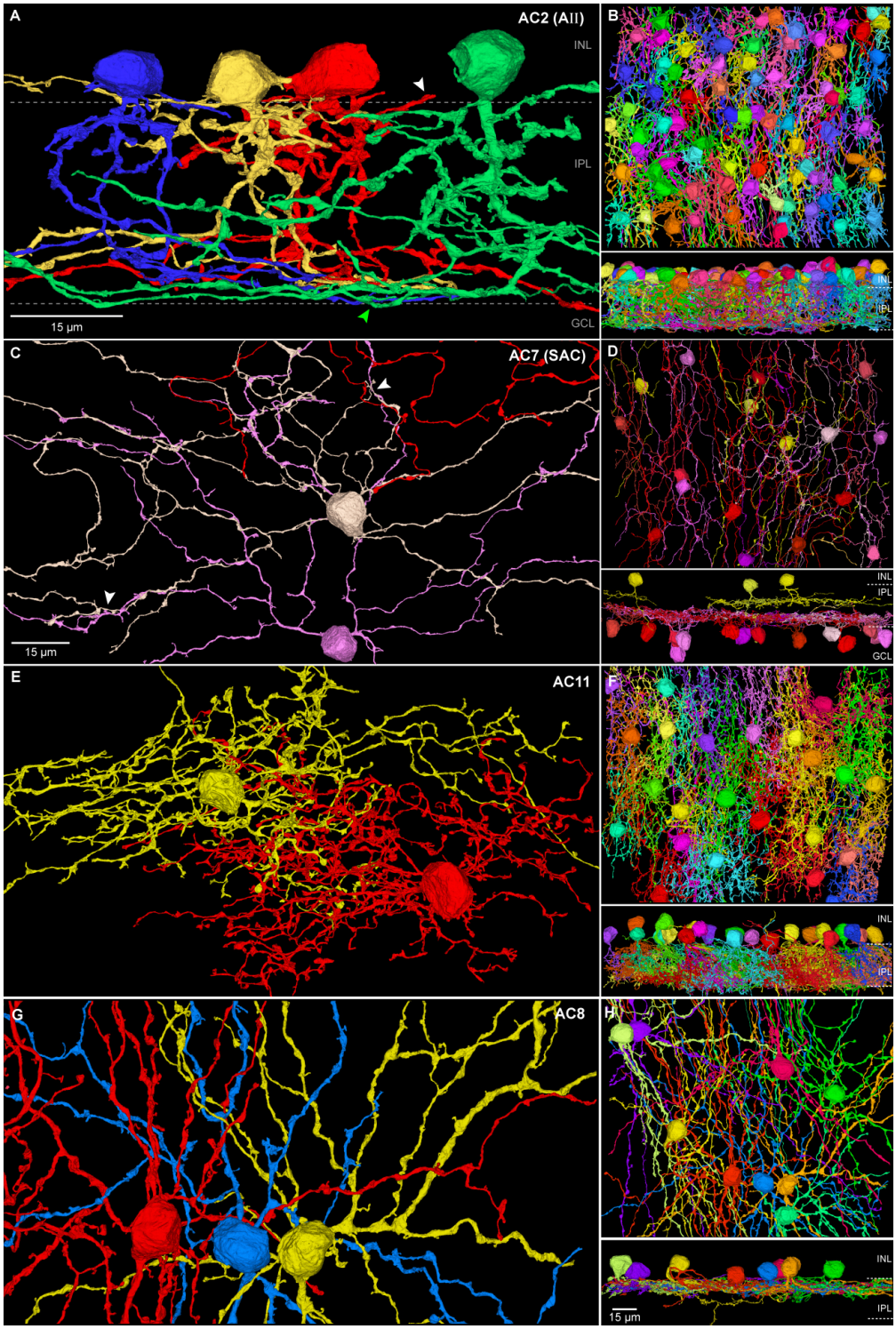

Fig. 5. Amacrine cells. Amacrine cells in the INL (253 cells) and GCL (40 cells) were divided into 19 types (AC1-19; *SI Appendix*, Table 1G). **A.** Small-field AII amacrine cells (AC2) shown in vertical view, with outer lobular dendrites (white arrowhead) and extensive inner dendrites (green arrowhead). **B.**

505 Horizontal view of the entire AII population in HFseg1. Lower panel: vertical view. **C.** Starburst
506 amacrine cells (AC7) were located primarily in the GCL (14 cells; INL, 3 cells). White arrowheads
507 indicate typical fasciculation of starburst dendrites. **D.** Mosaic of starburst cells, with GCL cells (red-
508 violet) and INL cells (yellow); lower panel: vertical view. **E**. Small-field amacrine cell type (AC11) in
509 horizontal view with densely branched dendritic arbor. **F**. Horizontal view of the AC11 cell mosaic; lower
510 panel: vertical view showing dendrites that extend broadly across the IPL. **G.** Large-field amacrine cells
511 (AC8) with thick lobular dendrites, narrowly stratified in the outer IPL. **H.** Horizontal view of the
512 complete mosaic; lower panel shows vertical view of outer IPL stratification. Scale bar in **C** applies to **E**
513 and **G**. Scale bar in lower panel of **H** applies to **B, D,** and **F**.

514

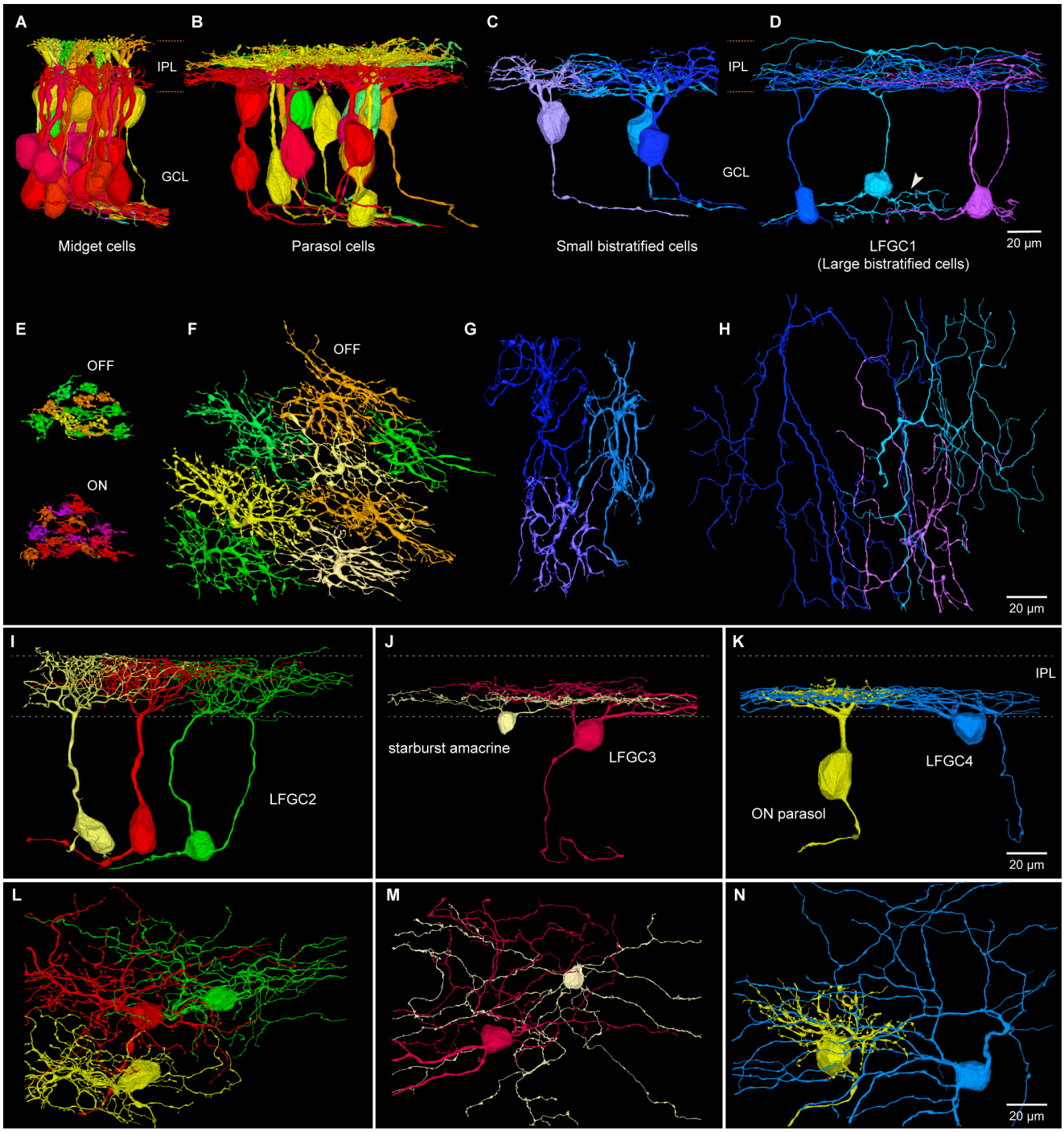

Fig. 6. Ganglion cells. A. Cluster of inner-ON (red-violet) and outer-OFF (yellow-green) midget ganglion cells; dendrites stratify broadly across inner (ON) and outer (OFF) halves of the IPL. **B**. Inner-ON (red-violet) and outer-OFF (yellow-green) parasol ganglion cells; dendrites stratify broadly near the center of the IPL. **C**. Small bistratified ganglion cells extend dendrites across the ON-OFF subdivision

520 of the IPL. **D**. Large bistratified ganglion cells (LFGC1) show large dendritic fields and broad
521 stratification. White arrowhead shows branching processes of unknown significance arising from the
522 cell body. **E-H**. Mosaics of dendritic arbors in horizontal view of the same cells shown in **A-D**. **E**. Outer-
523 OFF (yellow-green, top) and inner-ON (red-violet) midget GCs. **F**. Outer-OFF parasol cell dendrites
524 show minimal overlap (inner-ON parasol mosaic not shown). **G**. Small bistratified cells show minimal
525 dendritic tree overlap. **H**. LFGC1 (Large bistratified cells) show a much larger and more sparsely
526 branching irregular tree. **I-K**. Morphology of three additional large field types. **I**. LFGC2 (Large diffuse
527 cells) show a densely branched tree broadly stratified across the IPL. **J**. LFGC3 (Recursive bistratified
528 cells) are narrowly bistratified near the center of the IPL and tend to fasciculate with starburst amacrine
529 cells. **K**. LFGC4 (Inner smooth monostratified cells) show large, monostratified dendritic trees
530 costratified with parasol cells. **L-N**. Horizontal views of the cells shown in **I-K.**

531

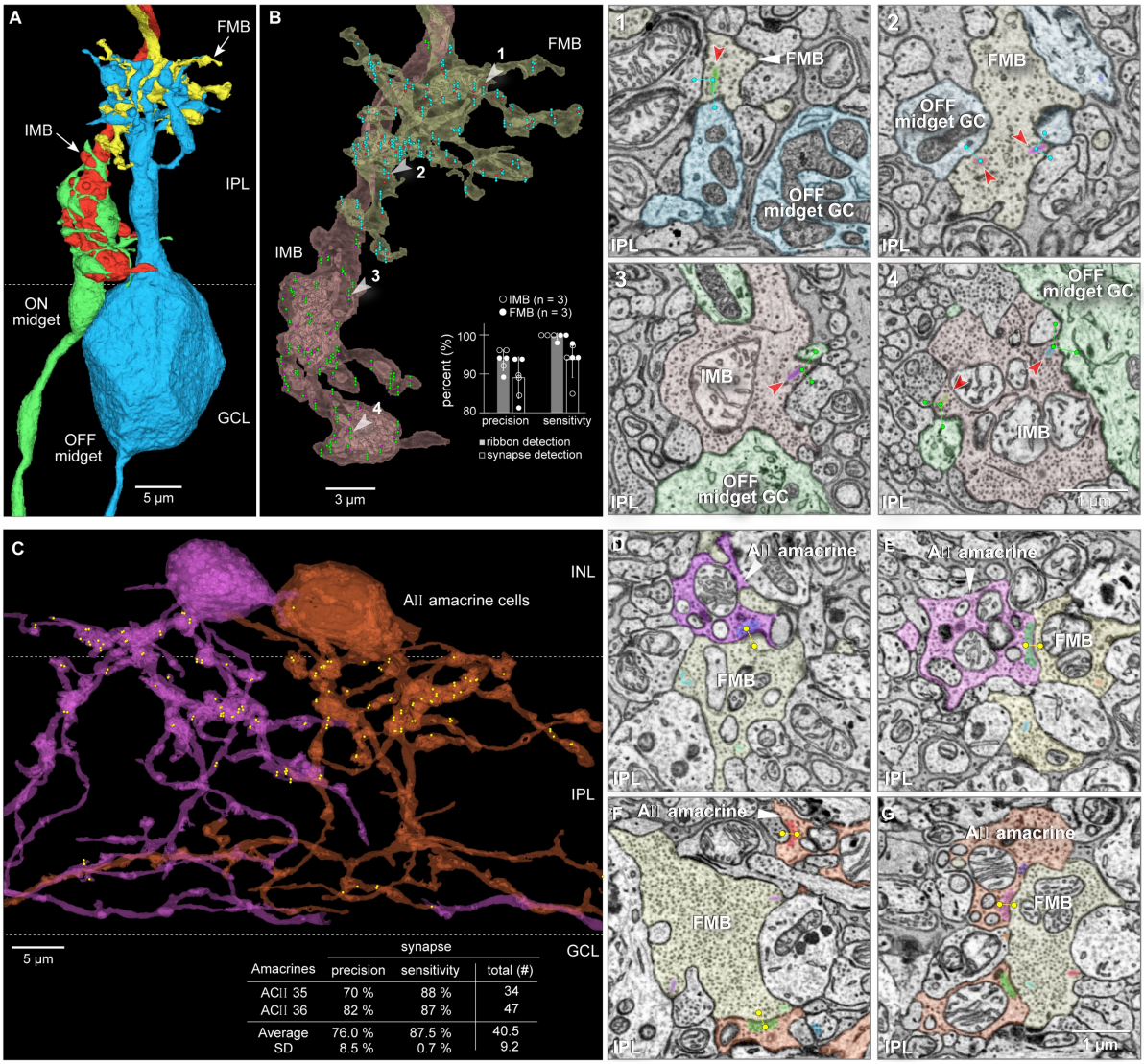

Amacrines	synapse precision	synapse sensitivity	synapse total (#)
ACII 35	70 %	88 %	34
ACII 36	82 %	87 %	47
Average	76.0 %	87.5 %	40.5
SD	8.5 %	0.7 %	9.2

Fig. 7. Synapse detection. A. OFF midget bipolar (yellow) and ON midget bipolar (red) presynaptic to an outer-OFF (blue) and inner-ON (green) midget ganglion cell. **B.** Outgoing synapses detected for the midget bipolar cell axon terminals shown in **A** (ganglion cells removed, semi-transparent view). Synaptic ribbons (red/violet dots) and postsynaptic profiles were first identified manually for cone 22, BC 308 (IMB), and BC 303 (FMB) (see *SI Appendix*, Fig. S9). Predicted outgoing synapses are shown as green dots and lines (IMB) or blue dots and lines (FMB). White arrowheads numbered 1-4 indicate the panels shown on the right in single-layer EM view, displaying segmented synaptic ribbons (in varied colors, red arrowheads) and predicted postsynaptic segments (dots and lines linking ribbons to postsynaptic structures); unlabeled postsynaptic profiles belong to amacrine cells. Inset histogram shows precision

542 and sensitivity of ribbon detection and synaptic assignment. **C.** Inhibitory output synapses made by two
543 neighboring AII amacrine cells (purple and orange, shown in partial transparency). Yellow dots show
544 predicted synaptic outputs; most synaptic outputs arise in the outer half of the IPL and are presynaptic to
545 OFF bipolar cells. Inset shows precision and sensitivity for the synapses made by each AII cell. **D-E**.
546 Single-layer images showing segmented vesicle clouds (varied colors) in the purple AII cell (shown in **C**)
547 and predicted synaptic connections with an FMB cell (yellow dots and lines); segmented ribbons in the
548 FMB are also shown. **F-G**. Single-layer images showing segmented vesicle clouds (varied colors) in the
549 orange AII cell (shown in **C**) and predicted synaptic connections with another FMB cell (yellow dots and
550 lines); segmented ribbons in the FMB are also shown.

551

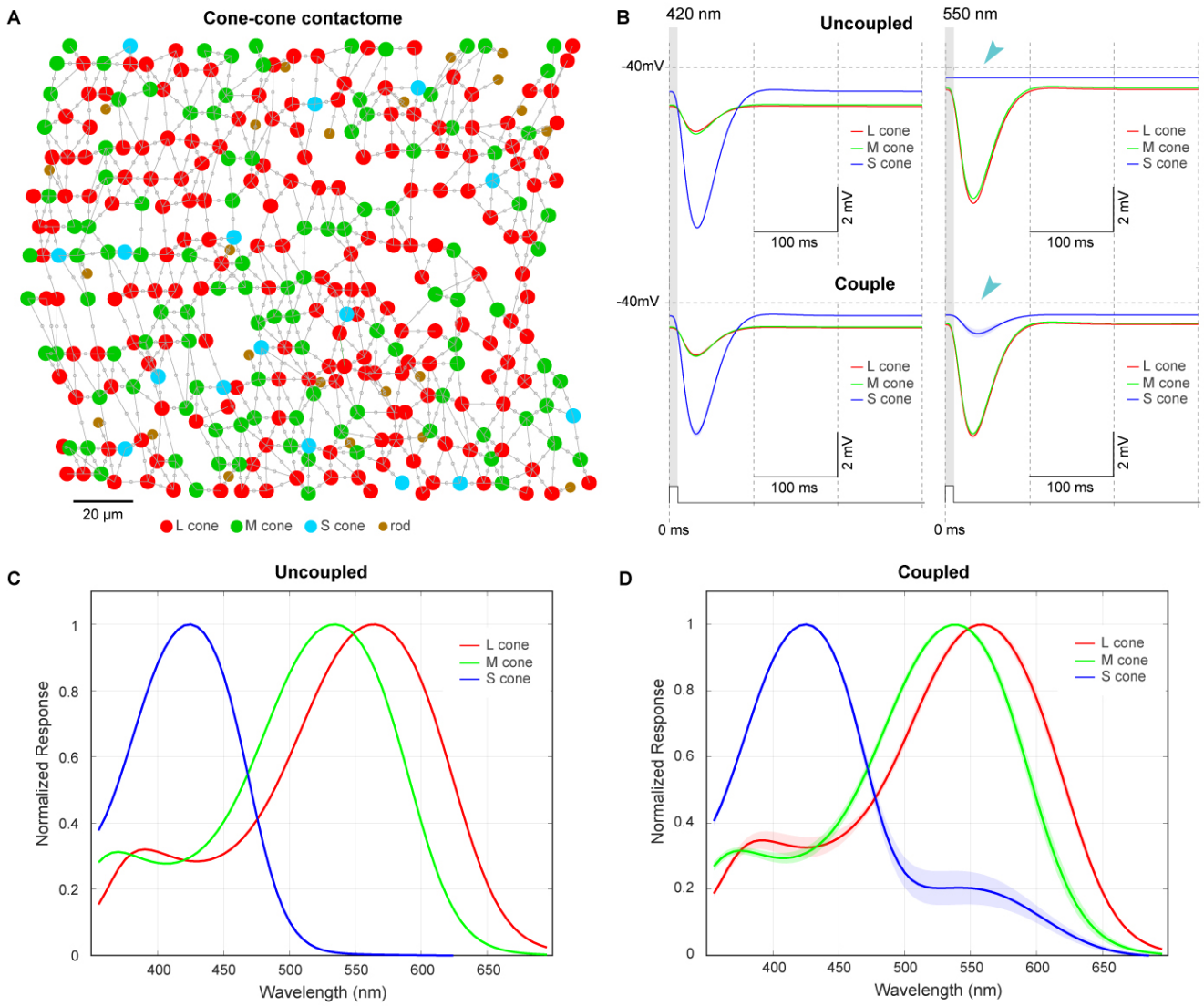

Fig. 8. Cone-cone coupling alters S cone spectral tuning. A. Biophysical model of the cone-cone connectome. Assignment of L/M cone type was random with a ~1.7:1 L:M ratio, based on known proportions in the human fovea. Contacts between cones were determined from the reconstructed connectome, and conductances were assigned based on the contact area, known gap junction density, and single connexin channel conductance. Cones were modeled compartmentally as a soma that included the phototransduction cascade, connected to an axon, in turn connected to the axon terminal (see model parameters in *SI Appendix*, Table 4). **B**. Modeled voltage responses (averages from 5 different L, M, and S cones in the network) to monochromatic 10 msec light flashes at 420 nm and 550 nm. **Top (Uncoupled):** zero cone-cone conductance. **Bottom (Coupled)**: cones coupled via individual cone-cone conductances

given in the electrical model. Coupling among L, M, and S cones produces a light-evoked response in S cones at 550 nm (teal arrowhead) that is absent in the uncoupled condition. **C**, **D**. Impact of cone-cone coupling on the action spectrum of the cone voltage response. Average light responses were generated every 5 nm from 350 to 700 nm. **C** (Uncoupled condition): the action spectrum is proportional to the spectral sensitivity of the L, M, and S cone opsins. **D** (Coupled condition): the S cone voltage response shows a smaller second peak of sensitivity at ~550 nm (teal arrowhead), which is not present when cones are uncoupled.

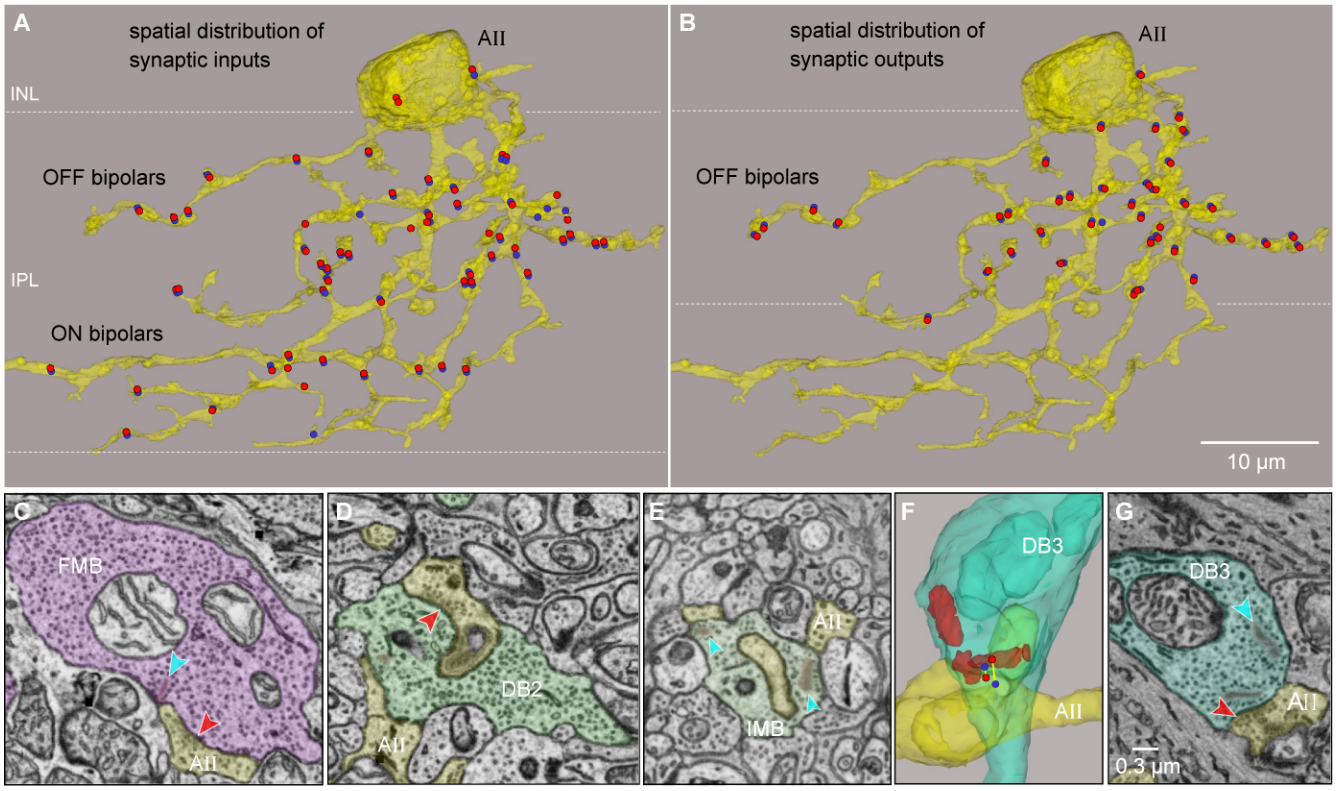

Fig. 9. AII cells are postsynaptic to both ON and OFF cone bipolar cells at ribbon synapses. A. Chemical (ribbon) synaptic inputs from multiple OFF and ON bipolar types. For this cell, 70 synapses (red dots, presynaptic locus; blue, postsynaptic locus; most blue postsynaptic dots are overlying the presynaptic position and are not visible in this zoomed-out view) are dispersed throughout the dendritic tree. Across 6 AII cells analyzed, 300 synapses arose from all ON and OFF cone bipolar types, with IMB and FMB cells accounting for 19% and 24% of the synapses, respectively. **B**. By contrast, this AII cell is presynaptic only to OFF cone bipolar cells; many of these synapses are reciprocal. **C**. An OFF-midget bipolar (FMB, violet) makes a ribbon dyad synapse (blue arrowhead points to ribbon) with the AII cell (yellow) and a parasol ganglion cell. The AII cell makes a nearby reciprocal synapse (red arrowhead) onto this FMB. **D.** Nonreciprocal AII synapse with a DB2 OFF bipolar type (teal). **E.** AII cell (yellow) postsynaptic to an ON-midget bipolar (IMB, green) at two dyad ribbon synapses (blue arrowheads). **F**. 3D view of a reciprocal synapse between this AII cell and a DB3 bipolar (blue); the AII cell inserts a finger-like projection into this bipolar axon terminal. **G**. Single section through contact in **F,**

584 showing two of the three ribbon synapses (blue arrowhead indicates one) and the reciprocal AII

585 inhibitory synapse (red arrowhead).

586

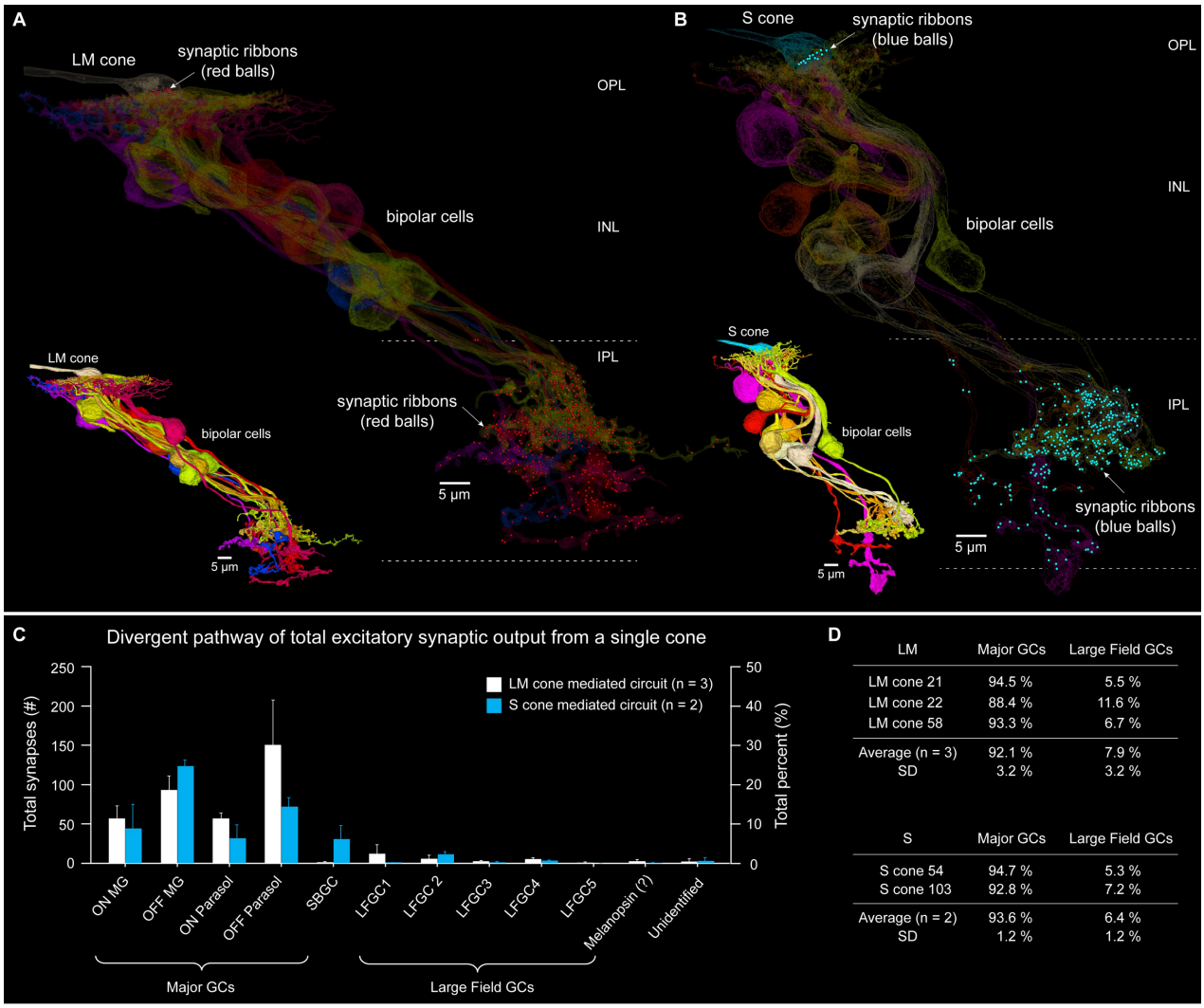

LM	Major GCs	Large Field GCs
LM cone 21	94.5 %	5.5 %
LM cone 22	88.4 %	11.6 %
LM cone 58	93.3 %	6.7 %
Average (n = 3)	92.1 %	7.9 %
SD	3.2 %	3.2 %

S	Major GCs	Large Field GCs
S cone 54	94.7 %	5.3 %
S cone 103	92.8 %	7.2 %
Average (n = 2)	93.6 %	6.4 %
SD	1.2 %	1.2 %

Fig. 10. Vertical excitatory connectome. A. Vertical connectome for a single LM cone (cone 22; see details in *SI Appendix*, Fig. S9B). Cone pedicle and postsynaptic bipolar cells shown in silhouette. Synaptic ribbons in the cone pedicle (top, OPL) and bipolar cell axon terminals (lower, IPL) are shown as red balls. Inset shows all bipolar cells postsynaptic to this cone pedicle (outer, yellow-gold; inner, blue-violet-red). **B**. The same views for an identified S cone (cone 103; see details in *SI Appendix*, Fig. S10B). Synaptic ribbons shown as blue balls. **C**. Histogram shows output synapse numbers (left axis) and percentage (right axis) made by bipolar cells connected to 3 LM and 2 S cones to postsynaptic GC types. Note that OFF-pathway-derived synapses greatly outnumber ON pathway synapses. **D**. The great majority of synapses from LM and S cones are distributed to midget, parasol, and small bistratified ganglion cells (Major GCs), with all other large-field types receiving 7.9% (LM) and 6.4% (S) of the

synaptic output (see also *SI Appendix*, Table 2). Unidentified processes account for 0.5% of the total synaptic output (LM) (see also *SI Appendix*, Table 2A-2C).

601 **Methods**

602 **EXPERIMENTAL MODEL AND SUBJECT DETAILS**

603 **Human tissue acquisition and preparation**

604 Human eyes (52-year-old, white male; brain dead organ donor) were acquired from the Medical
605 University of Vienna, Vienna, Austria at the time of death by surgical enucleation. A small incision was
606 made to give fixative access to the posterior chamber and the retina was in this way immersion fixed in
607 4% glutaraldehyde in 0.1 M sodium cacodylate buffer, pH7.3-7.4 at room temperature. Medical history
608 confirmed no abnormalities of the visual system recorded and no driving limitations; the ocular status
609 was defined medically as unremarkable at time of enucleation. Eyes were shipped in fixative to the
610 University of Washington where the retinas were dissected and prepared for electron microscopy.

611

612 **METHOD DETAILS**

613 **Identification of foveal ROI, serial block-face SEM sample preparation and image acquisition**

614 Retinal tissue was dissected under a dissecting microscope to facilitate identification of the optic disc
615 and the center of the foveal pit as well as the major retinal meridians. We selected an ROI that extends
616 across absolute eccentricity of ~450-650 microns (temporal retina). This location is linked to cones
617 located ~100-300 microns from the foveal pit center due to the lateral migration of retinal circuits from
618 the cones at the foveal center. This location encompasses much of the central 1 degree (~300 μm/deg)
619 of visual angle (Fig. 1A-1C).

620 The dissected retina was then plastic embedded and prepared for electron microscopy as previously
621 described[1]. In brief, the tissue was incubated in a 1.5% potassium ferrocyanide and 2% osmium
622 tetroxide (OsO4) solution for 1 h. After washing, the tissue was placed in a freshly made
623 thiocarbohydrazide solution for 20 min and then rinsed and incubated in 2% OsO4 for 30 min. Lastly,
624 the tissue was stained en bloc in 1% uranyl acetate overnight and subsequently stained with Walton's

625 lead aspartate, dehydrated and plastic embedded (Durcupan, 44610, Sigma Aldrich). After evaluation
626 of the ROI by semithin sectioning the tissue block was trimmed, gold-coated by standard methods, and
627 mounted in an Apreo SEM Volumescope (Thermo Fisher). We cut 3028 sections at 50 nm thick for a
628 total depth of ~150 microns, imaging an ROI (180 μm tall x 180 μm wide; 5 nm pixels) that
629 encompassed the full vertical depth of the retina, from the Henle fiber layer (HFL) to the nerve fiber
630 layer (Fig. 1D). The overall ROI was imaged on the blockface after each section as 25 sequential tiles
631 (8000 x 8000 pixels or 40 x 40 μm; 75,700 total image tiles) with 10% overlap. Images were stitched
632 within layer and aligned across layers using standard methods available in TrakEM2[2] (NIH image
633 plugin; Scale Invariant Feature Transform (SIFT) with affine translation) to create a good quality
634 volume. We first evaluated this TrakEM2-aligned volume by manual reconstruction of a small number of
635 selected cells and circuits(106). To further develop this volume as a connectomic resource we applied
636 deep-learning based computational approaches to realign, segment and reconstruct all cells and
637 synaptic connections as follows(20, 39).

638 **Volume creation**

639 *Montaging.* Tile offsets were determined manually, then refined by template matching at 40 nm with a
640 search window of 96 pixels. Tiles were cropped by 128 pixels to avoid edge distortions and placed to
641 minimize the sum of least squares from the new offsets. Outliers were inspected and given manual
642 placement. These cropped tiles were processed to create a pyramid of encodings for resolutions
643 between 20 nm and 640 nm(107), and then stitched to make the montaged section in two steps. In the
644 first step, only the two neighboring tiles in Y were considered, with both neighbors being fixed. Using an
645 online finetuner pyramid(107) with the calculated placement as the starting point, a displacement field
646 was generated that would warp the encoded tiles to minimize the pixel difference with the fixed tiles.
647 The encoded tiles were then warped using this displacement field, eroded by a pixel to avoid partial
648 pixels at the edge, blended to the fixed tiles using the mean of the pixel values in the overlap, and then
649 passed through CLAHE (Contrast Limited Adaptive Histogram Equalization) enhancement to mitigate

650 the contrast loss from the warping and blending, resulting in strips of encoded tiles where every other
651 tile had been warped. In the second step, the strips of tiles from the first step were stitched to each
652 other, holding every other strip fixed in a similar process. An error map was generated at both steps by
653 computing the difference between the encodings in the overlap at 40 nm and inspected. The non-
654 encoded tiles were cropped by 394 pixels, warped according to the composed displacement fields from
655 the encodings, and combined to yield montaged sections.

656 *Alignment.* The unaligned sections were first processed to create a pyramid of encodings(107). A rigid
657 transformation for the entire dataset was estimated using SIFT features(108) extracted from the
658 encodings at 640 nm and correspondences established between nearest and next-nearest section pairs.
659 From the rigidly aligned encodings, displacement fields at 40 nm resolution were generated between
660 nearest and next-nearest section pairs using an online finetuner pyramid(107).

661 A convolutional net trained to detect local misalignments and/or simple mismatches caused by defects
662 in the EM images was used to mask unreliable regions in each displacement field. In addition, 25
663 sections with defects that presented with non-smooth deformations were masked by hand. Pairwise
664 displacement fields and transformation masks were then passed to a global relaxation(107, 109). This
665 relaxation was performed first at 2560 nm across all 3028 sections of the dataset, and subsequently in
666 blocks of approximately 100 sections at a resolution of 640 nm, using the previously generated drift-free
667 fields as constraints for the start and end sections of each of the 31 blocks. The resulting displacement
668 fields were composed with the earlier rigid transformation and the final aligned image stack warped and
669 rendered at 10 nm.

670 *Segmentation.* We pretrained a convolutional net to predict affinities between neighboring voxels at
671 16×16×40 nm^3 using 1,368 μm^3 of manually annotated data derived from three mouse visual cortex
672 datasets(110). We used the residual symmetric U-Net architecture(111) with modifications(112) and
673 trained with data augmentation previously described (113). The network was trained for 2,000,000

674 iterations using four NVIDIA L4 GPUs with PyTorch data parallelism, where each GPU processed
675 individual patches with its own model replica.

676 To further fine-tune this network, we manually created training data consisting of 39 μm^3 at a resolution
677 of $20 \times 20 \times 50$ nm^3. In contrast to the pretraining datasets, mitochondria were intentionally over
678 segmented to bias boundary detection toward a more conservative approach, aiming primarily to
679 reduce merge errors at the expense of increasing split errors. We fine-tuned the network for 300,000
680 iterations.

681 We predicted an affinity map for the whole dataset. Dark voxels could sometimes span multiple cells
682 and cause segmentation errors. We therefore applied a binarized mask for dark voxels with a threshold
683 of 0.2, invalidating each dark voxel and its three incident affinities. The resulting masked affinity map
684 was then segmented with a mean affinity agglomeration threshold of 0.25(113). The segmentation was
685 ingested into the Connectome Annotation Versioning Engine proofreading platform, CAVE(114) for
686 further analysis.

687 CAVE permitted proofreading to be performed by a user community accessing the web-based
688 neuroglancer interface(113, 115) with dynamic updating of segment ID and related synaptic
689 connectivity. The HFseg 1 segmentation was of high initial quality such that it was possible to identify
690 and annotate all major cell classes within the volume and to sort these cells into populations of distinct
691 types using the annotation tools available in neuroglancer. All cells are accessible at NeuroMaps
692 (https://neuromaps.app).

693 Cell types were identified provisionally based on segment 3D morphology (dendritic morphology,
694 stratification depth, and spatial regularity and interaction (mosaics) and in some cases nuclear
695 morphology). Four of the authors (Kim, Dacey, Grünert and Martin) conferred and agreed on cell type
696 identification. Proofreading is ongoing (~ 40,000 edits) and applied thus far primarily to correct larger
697 obvious mergers (primarily with glial cell processes) that interfered with cell type identification and

698 additional more detailed proofreading on circuits of interest in the current survey of cone-bipolar-
699 ganglion cell connections. Many cell populations were unambiguously recognized based on previous
700 studies of primate retina(41, 116, 117) (e.g., the S cones, rods and LM cones, the H1 and H2 horizontal
701 cells, the starburst and AII amacrine cell types, the midget, diffuse, blue-cone bipolar, and rod bipolar
702 types, or the midget, parasol and small bistratified and large bistratified ganglion cell types; Müller glia,
703 astrocytes and microglia); some cell types (the low-density amacrine types) were provisionally
704 designated subject to further proofreading and connectivity analysis. Following FlyWire(40), we have
705 initiated an open community of retinal neurobiologists (currently 7 labs participating) to use these tools
706 to complete proofreading of the HFseg1 volume.

707 **Synapse detection**

708 *Ribbon synapse detection in OPL and IPL*. A symmetric residual U-Net architecture was trained on
709 data with a resolution of 10×10×50 nm^3 using input patches of size 128×128×20 to generate a
710 probability map that indicates the likelihood of each voxel belonging to a synaptic ribbon (118). To
711 remove less robust predictions at the boundaries, only the central 96×96×16 voxels of the input
712 patch was used as the output. The model was trained on a total volume of 2,254 μm^3 of manually
713 labeled cutouts sampled from various regions across the entire dataset.

714 The ribbon segmentation was produced by (1) down sampling the probability map by 2×, (2)
715 thresholding for voxels above 0.15, and (3) using 26-connectivity to extract connected components.
716 Segments smaller than 5 voxels in a 20×20×50 nm^3 resolution were neglected to eliminate spurious
717 detections.

718 To achieve ribbon detection in the OPL segments smaller than 5 voxels (in a 20×20×50 nm^3 resolution
719 volume) were first disregarded to eliminate spurious detections of extremely small ribbon-like
720 structures. For each detected ribbon within a cone pedicle, postsynaptic partners were identified via the

721 following steps: (1) All neighboring segments touching the pedicle within 800 nm of the ribbon centroid
722 were identified. (2) For each neighbor, a representative point close to the ribbon was chosen as the
723 postsynaptic site. These constitute the set of putative synapses for each ribbon. (3) After cell
724 identification, only putative synapses onto bipolar or horizontal cells were kept; all others were filtered
725 out (e.g. Müller glia, neighboring cones, mitochondria). (4) Finally, for each distinct ribbon-postsynaptic
726 cell pair, all but the shortest putative synapse were filtered out. The result was that a single synaptic
727 connection was found onto any bipolar or horizontal cell contacting that cone pedicle within 800 nm of a
728 given cone ribbon.

729 For synaptic ribbons in the IPL, segments smaller than 5 voxels in a 20×20×50 nm^3 resolution within
730 the bounds of the IPL were also disregarded to eliminate spurious detections. For each detected
731 ribbon, postsynaptic partners were automatically identified via the following steps: (1) Identify the two
732 largest cells within a small (500 nm) window of the centroid of the ribbon which are adjacent to the
733 presynaptic cell and are also adjacent to each other. (2) If such a pair is found, the ribbon is assumed to
734 be presynaptic to both (i.e., a dyadic synapse). (3) If no such pair is found, then within the window, the
735 single largest profile adjacent to the presynaptic cell is identified as the postsynaptic partner. (4)
736 Putative synaptic connections were filtered by cell type, requiring the presynaptic cell to be previously
737 annotated as a bipolar cell, and the postsynaptic partner to be previously annotated as amacrine, or
738 ganglion cell. Note we did not at this time try to use a convolutional net to detect a low density of
739 possibly ribbonless synapses.

Vesicle cloud detection and conventional synapse assignment in the IPL. A symmetric residual U-Net architecture was trained on data with a resolution of 10×10×50 nm^3 using input patches of size 128×128×20 to generate a probability map that indicates the likelihood of each voxel belonging to a vesicle cloud(118). To remove less robust predictions at the boundaries, only the central 96×96×16 voxels of the input patch was used as the output. The model was trained on a total volume of 2,254 μm^3 of manually labeled cutouts sampled from various regions across the entire dataset (the same cutouts as ribbon synapse detection). Manual labels were roughly annotated to mark approximate locations of vesicle clouds rather than precise boundaries.

The vesicle cloud segmentation was produced by (1) downsampling the probability map by 2×, (2) thresholding for voxels above 0.15, and (3) using 26-connectivity to extract connected components. Segments with fewer than 200 voxels were excluded, based on the range of vesicle cloud sizes encountered.

IPL conventional synapse assignment. A symmetric residual U-Net architecture was trained on data with a resolution of 20×20×50 nm^3 using input patches of size 24×24×8 to generate a probability map that indicates the likelihood of each voxel belonging to the postsynaptic cell(118). The model was trained on 682 μm^3 of manually annotated labeled cutouts.

The model was applied once for each vesicle cloud detected, in a window centered on the centroid of the vesicle cloud. Using the initial automatic cell segmentation, the cell with the highest mean probability within the window was selected as the putative postsynaptic partner(118). Further filtering by cell type was applied, requiring the presynaptic cell to be previously annotated as an amacrine cell, and the postsynaptic partner to be previously annotated as amacrine, bipolar, or ganglion cell.

Building and modeling the cone-cone contactome

Generating the cone-cone contactome. We identified gap junctions between cone pedicles and between cone pedicles and rods as follows. Cones and rods were manually identified and proofread to

764 completion. Contacts were computed using a recently developed supervoxel agglomeration process
765 (abiss)(119) where a contact is considered to be a set of connected voxel faces that are shared by the
766 same pair of segments. For each contact, we counted the number of voxel faces along each orientation
767 (xy, xz, and yz), as well as the minimum bounding box containing all of the faces. The surface area of a
768 contact was estimated by computing the sum of the area of all faces involved. Contacts were excluded
769 from analysis if (1) the surface area of the contact was $\leq$0.04 μm^2 (mean surface area of contact, 0.55
770 ± 0.3 μm^2, n = 1141 cone-cone contacts) or (2) the center of the bounding box was more than 15 μm
771 from the approximate center of the cone pedicle (manually identified). All remaining contacts were
772 manually inspected with 1× coverage to determine if they corresponded to what would be manually
773 identified as a true cone-cone contacts harboring gap junctions.

774 *Biophysical modeling of cone-cone contactome***.** To generate a biophysical model of the electrically
775 coupled photoreceptor network, we started with data from the X,Y locations of 310 cone and 24 rod
776 synaptic terminals, and for the cones their M/L vs. S identity. We then incorporated all reviewed and
777 accepted cone-cone contacts and the surface areas of each contact.
778

779 The cone morphology was modeled as a sphere (single compartment, dia. 2.5 μm) for the outer and
780 inner segments and soma, connected to an axon (dia. 1.6 μm, Ri 80 Ohm-cm, Rm 12,000 Ohm-cm^2
781 (120); V_{rev} -60 mV, compartment size 0.05 lambda, ~9 compartments/cone axon) extending 300 μm to
782 the terminal (diam 5 μm, Rm 12,000 Ohm-cm^2, V_{rev} -60mV). Rod morphology was similar (OS/IS diam
783 2.5 μm, axon dia 0.45 μm, terminal dia. 3 μm). The OS/IS/soma compartment contained a transduction
784 mechanism (max conductance 880 pS) with spectral sensitivity appropriate for the cone identity. The
785 transduction mechanism of the photoreceptor biochemical cascade generated a peak ~20 ms after the
786 stimulus with a damped recovery (121-128). Spectral sensitivity for the L/M cones was taken from
787 macaque monkey (128) and for the S cones from human cone data (peak sens. 420 nm (129) corrected

788 for lens spectral sensitivity (130)). In some models including both lens and macular filters, the S cone
789 peak sensitivity was shifted to ~440 nm.
790
791 The location of all the S-cones and rods in the reconstructed contactome was known but the individual
792 identity of L/M cones was unknown, so for the simulations the L/M identity was set randomly. The target
793 L/M ratio was 1.7 and the actual L/M ratio in the model shown was 1.697. The contacts between cones
794 had not been resolved into gap junctions (groups of connnexin molecules), but the area of each contact
795 had been measured. The conductance for each contact was calculated by taking the average area of
796 the contacts (0.55 μm^2), assuming 5 connexins (69) (15 pS per connexin) per average contact (131,
797 132) to produce an average conductance of 75 pS, or 136 pS/μm^2. The conductance for each individual
798 contact was then calculated by multiplying by the contact area. Contacts were simulated with a linear
799 gap junction conductance (i.e. electrical synapse). The cones had on average 3.6 contacts with
800 neighboring cones. The average L/M total coupling conductance was ~270 pS, and for S-LM cones was
801 ~282 pS. There were a total of 715 coupled pairs of cones, 659 LM pairs, and 56 pairs with 1 S cone.
802 The average coupling conductance between adjacent pairs of L/M cones was 116 pS, and for L/M–S
803 pairs was 123 pS. However, the average measured coupling conductance between LM pairs was 133
804 pS (n = 25) and between S-LM pairs was 166 pS (n = 14) due to the existence of multiple current paths
805 between pairs through the gap junction network. The average cone terminal input resistance was ~0.4
806 Gohm.
807
808 The simulated cones were stimulated with flashes of monochromatic light (10 ms, 1000 μm spot, ~1 x
809 10^5 photons/μm^2/sec) on a white background (1 x 10^4 photons/μm^2/s, spectrally flat). The resting
810 potential V_{rest} in response to the background was ~ -40 mV but varied by ~0.3mV depending on the
811 cone identity and coupling. The flash response varied from 0 to -5 mV. To determine the effect of the
812 gap junctions, simulations were run with the gap junction conductance at 0%, 50%, 100%, and
813 multiples of the nominal 136pS/μm^2 conductance. The model was constructed in the Neuron-C

simulation language (133) and comprised ~3000 compartments. The model was run on AMD Opteron 3000 MHz CPUs under the Linux and Mosix operating systems. Approximately 200 simulations were run of the 310-cone model to develop and calibrate the model. Modeling code can be accessed at zenodo.org upload of Neuron-C at: https://doi.org/10.5281/zenodo.17792059.

Proofreading, synaptic connectivity and updating with the Connectome Annotation Versioning Engine (CAVE) and NeuroMaps.

As noted above we ingested synapse predictions and cell type annotations into CAVE. A critical functionality given by CAVE is that is allows collaborative users to programmatically query the up-to-date proofread connectivity graph (synaptic connectivity is updated during proofreading of each segment-cell type) as well as any changes made to the metadata (cell type IDs, descriptions, or other annotations). We then adapted NeuroMaps to combine this metadata with synaptic connectivity for each segment ID and to permit synaptic proofreading (addition or deletion of specific synaptic predictions).

DATA AND SOFTWARE AVAILABILITY

The HFseg1 dataset (volume, segmentation, synaptic detection and full annotation) are currently hosted by Zetta.ai (https://zetta.ai/) and all data is accessible for community proofreading by permission at NeuroMaps. The latest version of the HFseg1 dataset is also available for interrogation at NeuroMaps (https://neuromaps.app). Modeling code can be accessed at zenodo.org upload of Neuron-C at: https://doi.org/10.5281/zenodo.17792059

838 **References**

839 1. S. Ramon y Cajal, La rètine des vertèbrès. *La Cellule* **9**, 119-257 (1892).

840 2. R. H. Masland, E. Raviola, Confronting complexity: strategies for understanding the
841 microcircuitry of the retina. *Annual review of neuroscience* **23**, 249-284 (2000).

842 3. J. E. Dowling, *The Retina: An approachable part of the brain* (Harvard University Press,
843 Cambridge, MA, ed. 2nd, 2012), doi.org/10.2307/j.ctv31zqj2d, pp. 384.

844 4. R. W. Rodieck, *The First Steps in Seeing* (Sinauer Associates, Inc., Sunderland MA, 1998), pp.
845 562 pp.

846 5. M. Helmstaedter *et al.*, Connectomic reconstruction of the inner plexiform layer in the mouse
847 retina. *Nature* **500**, 168-174 (2013).

848 6. J. S. Kim *et al.*, Space-time wiring specificity supports direction selectivity in the retina. *Nature*
849 **509**, 331-336 (2014).

850 7. K. L. Briggman, M. Helmstaedter, W. Denk, Wiring specificity in the direction-selectivity circuit of
851 the retina. *Nature* **471**, 183-188 (2011).

852 8. J. R. Anderson *et al.*, Exploring the retinal connectome. *Molecular vision* **17**, 355-379 (2011).

853 9. D. J. Calkins, S. J. Schein, Y. Tsukamoto, P. Sterling, M and L cones in macaque fovea connect
854 to midget ganglion cells by different numbers of excitatory synapses. *Nature* **371**, 70-72 (1994).

855 10. D. J. Calkins, P. Sterling, Absence of spectrally specific lateral inputs to midget ganglion cells in
856 primate retina. *Nature* **381**, 613-615 (1996).

857 11. K. Shekhar *et al.*, Comprehensive Classification of Retinal Bipolar Neurons by Single-Cell
858 Transcriptomics. *Cell* **166**, 1308-1323 e1330 (2016).

859 12. Y. R. Peng *et al.*, Molecular Classification and Comparative Taxonomics of Foveal and
860 Peripheral Cells in Primate Retina. *Cell* **176**, 1222-1237 (2019).

861 13. W. Yan *et al.*, Cell Atlas of The Human Fovea and Peripheral Retina. *Sci Rep* **10**, 9802 (2020).

862 14. J. Hahn *et al.*, Evolution of neuronal cell classes and types in the vertebrate retina. *Nature* **624**,
863 415-424 (2023).

864 15. J. Li *et al.*, Integrated multi-omics single cell atlas of the human retina. *Res Sq* 10.21203/rs.3.rs-
865 3471275/v1 (2023).

16. S. Dorkenwald *et al.*, Neuronal wiring diagram of an adult brain. *Nature* **634**, 124-138 (2024).

17. A. Azevedo *et al.*, Connectomic reconstruction of a female Drosophila ventral nerve cord. *Nature* **631**, 360-368 (2024).

18. A. Shapson-Coe *et al.*, A petavoxel fragment of human cerebral cortex reconstructed at nanoscale resolution. *Science* **384**, eadk4858 (2024).

19. S. Loomba *et al.*, Connectomic comparison of mouse and human cortex. *Science* **377**, eabo0924 (2022).

20. N. L. Turner *et al.*, Reconstruction of neocortex: Organelles, compartments, cells, circuits, and activity. *Cell* **185**, 1082-1100 e1024 (2022).

21. Z. Ding *et al.*, Functional connectomics reveals general wiring rule in mouse visual cortex. *Nature* **640**, 459-469 (2025).

22. L. F. Abbott *et al.*, The Mind of a Mouse. *Cell* **182**, 1372-1376 (2020).

23. J. W. Lichtman, J. R. Sanes, Ome sweet ome: what can the genome tell us about the connectome? *Current opinion in neurobiology* **18**, 346-353 (2008).

24. B. A. Wandell, S. O. Dumoulin, A. A. Brewer, Visual field maps in human cortex. *Neuron* **56**, 366-383 (2007).

25. M. I. Sereno, M. R. Sood, R. S. Huang, Topological Maps and Brain Computations From Low to High. *Frontiers in systems neuroscience* **16**, 787737 (2022).

26. B. M. Harvey, S. O. Dumoulin, The relationship between cortical magnification factor and population receptive field size in human visual cortex: constancies in cortical architecture. *J Neurosci* **31**, 13604-13612 (2011).

27. M. I. Sereno *et al.*, Borders of multiple visual areas in humans revealed by functional magnetic resonance imaging. *Science* **268**, 889-893 (1995).

28. M. M. Schira, C. W. Tyler, M. Breakspear, B. Spehar, The foveal confluence in human visual cortex. *J Neurosci* **29**, 9050-9058 (2009).

29. T. Baden *et al.*, The functional diversity of retinal ganglion cells in the mouse. *Nature* **529**, 345-350 (2016).

30. J. A. Bae *et al.*, Digital Museum of Retinal Ganglion Cells with Dense Anatomy and Physiology. *Cell* **173**, 1293-1306 e1219 (2018).

31. J. Goetz *et al.*, Unified classification of mouse retinal ganglion cells using function, morphology, and gene expression. *Cell reports* **40**, 111040 (2022).

32. R. A. Masri, K. A. Percival, A. Koizumi, P. R. Martin, U. Grünert, Survey of retinal ganglion cell morphology in marmoset. *J Comp Neurol* **527**, 236-258 (2019).

33. Y. J. Kim *et al.*, Origins of direction selectivity in the primate retina. *Nature communications* **13**, 2862 (2022).

34. C. A. Curcio, K. R. Sloan, R. E. Kalina, A. E. Hendrickson, Human photoreceptor topography. *J.Comp.Neurol.* **292**, 497-523 (1990).

35. C. A. Curcio, D. Kar, C. Owsley, K. R. Sloan, T. Ach, Age-Related Macular Degeneration, a Mathematically Tractable Disease. *Investigative ophthalmology & visual science* **65**, 4 (2024).

36. S. J. Schein, Anatomy of macaque fovea and spatial densities of neurons in foveal representation. *J Comp Neurol* **269**, 479-505 (1988).

37. N. Drasdo, C. L. Millican, C. R. Katholi, C. A. Curcio, The length of Henle fibers in the human retina and a model of ganglion receptive field density in the visual field. *Vision Res* **47**, 2901-2911 (2007).

38. R. A. Masri, U. Grünert, P. R. Martin, Analysis of Parvocellular and Magnocellular Visual Pathways in Human Retina. *J Neurosci* **40**, 8132-8148 (2020).

39. K. Lee *et al.*, Convolutional nets for reconstructing neural circuits from brain images acquired by serial section electron microscopy. *Current opinion in neurobiology* **55**, 188-198 (2019).

40. S. Dorkenwald *et al.*, FlyWire: online community for whole-brain connectomics. *Nature methods* **19**, 119-128 (2022).

41. U. Grünert, P. R. Martin, Cell types and cell circuits in human and non-human primate retina. *Progress in retinal and eye research* 10.1016/j.preteyeres.2020.100844, 100844 (2020).

42. U. Grünert, P. R. Martin, Morphology, Molecular Characterization, and Connections of Ganglion Cells in Primate Retina. *Annu Rev Vis Sci* **7**, 73-103 (2021).

920 43. L. Zhang *et al.*, Evolutionary and developmental specialization of foveal cell types in the
921 marmoset. *Proceedings of the National Academy of Sciences of the United States of America*
922 **121**, e2313820121 (2024).

923 44. Y. J. Kim *et al.*, Comparative connectomics reveals noncanonical wiring for color vision in
924 human foveal retina. *Proceedings of the National Academy of Sciences of the United States of*
925 *America* **120**, e2300545120 (2023).

926 45. D. M. Dacey, The mosaic of midget ganglion cells in the human retina. *J.Neurosci.* **13**, 5334-
927 5355 (1993).

928 46. D. M. Dacey, Morphology of a small-field bistratified ganglion cell type in the macaque and
929 human retina. *Visual neuroscience* **10**, 1081-1098 (1993).

930 47. D. M. Dacey, B. B. Lee, The blue-ON opponent pathway in primate retina originates from a
931 distinct bistratified ganglion cell type. *Nature* **367**, 731-735 (1994).

932 48. E. J. Chichilnisky, D. A. Baylor, Receptive-field microstructure of blue-yellow ganglion cells in
933 primate retina. *Nat.Neurosci.* **2**, 889-893 (1999).

934 49. D. J. Calkins, Y. Tsukamoto, P. Sterling, Microcircuitry and mosaic of a blue-yellow ganglion cell
935 in the primate retina. *J.Neurosci.* **18**, 3373-3385 (1998).

936 50. R. A. Masri, U. Greferath, E. L. Fletcher, P. R. Martin, U. Grünert, Immunohistochemistry and
937 spatial density of Müller cells in the human fovea. *Investigative ophthalmology & visual science*
938 **in press** (2025).

939 51. J. Singaravelu, L. Zhao, R. N. Fariss, T. M. Nork, W. T. Wong, Microglia in the primate macula:
940 specializations in microglial distribution and morphology with retinal position and with aging.
941 *Brain Struct Funct* **222**, 2759-2771 (2017).

942 52. M. Goyal, A. S. Bordt, J. Neitz, D. W. Marshak, Trogocytosis of neurons and glial cells by
943 microglia in a healthy adult macaque retina. *Sci Rep* **13**, 633 (2023).

944 53. S. Haverkamp, U. Grünert, H. Wassle, The cone pedicle, a complex synapse in the retina.
945 *Neuron* **27**, 85-95 (2000).

946 54. C. P. Grabner *et al.*, Mechanisms of simultaneous linear and nonlinear computations at the
947 mammalian cone photoreceptor synapse. *Nature communications* **14**, 3486 (2023).

948 55. S. Herr *et al.*, Cone synapses in macaque fovea: II. Dendrites of OFF midget bipolar cells
949 exhibit Inner Densities similar to their Outer synaptic Densities in basal contacts with cone
950 terminals. *Visual neuroscience* **28**, 17-28 (2011).

951 56. E. Strettoi, E. Raviola, R. F. Dacheux, Synaptic connections of the narrow-field, bistratified rod
952 amacrine cell (AII) in the rabbit retina. *J.Comp.Neurol.* **325**, 152-168 (1992).

953 57. E. Strettoi, R. A. Masri, U. Grünert, AII amacrine cells in the primate fovea contribute to photopic
954 vision. *Sci Rep* **8**, 16429 (2018).

955 58. H. Wässle, U. Grünert, M. H. Chun, B. B. Boycott, The rod pathway of the macaque monkey
956 retina: Identification of AII-amacrine cells with antibodies against calretinin. *J.Comp.Neurol.*
957 **361**, 537-551 (1995).

958 59. U. Grünert, Anatomical evidence for rod input to the parvocellular pathway in the visual system
959 of the primate. *Eur.J.Neurosci.* **9**, 617-621 (1997).

960 60. E. P. Hornstein, J. Verweij, J. L. Schnapf, Electrical coupling between red and green cones in
961 primate retina. *Nature neuroscience* **7**, 745-750 (2004).

962 61. J. J. O'Brien, X. Chen, P. R. Macleish, J. O'Brien, S. C. Massey, Photoreceptor coupling
963 mediated by connexin36 in the primate retina. *J Neurosci* **32**, 4675-4687 (2012).

964 62. L. E. Wool, O. S. Packer, Q. Zaidi, D. M. Dacey, Connectomic identification and three-
965 dimensional color tuning of S-OFF midget ganglion cells in the primate retina. *J Neurosci* **39**,
966 7893-7909 (2019).

967 63. T. D. Lamb, E. J. Simon, The relation between intercellular coupling and electrical noise in turtle
968 photoreceptors. *J Physiol* **263**, 257-286 (1976).

969 64. M. Tessier-Lavigne, D. Attwell, The effect of photoreceptor coupling and synapse nonlinearity on
970 signal:noise ratio in early visual processing. *Proc R Soc Lond B Biol Sci* **234**, 171-197 (1988).

971 65. S. H. DeVries, X. Qi, R. Smith, W. Makous, P. Sterling, Electrical coupling between mammalian
972 cones. *Current biology : CB* **12**, 1900-1907 (2002).

973 66. A. Hsu, R. G. Smith, G. Buchsbaum, P. Sterling, Cost of cone coupling to trichromacy in primate
974 fovea. *Journal of the Optical Society of America. A, Optics, image science, and vision* **17**, 635-
975 640 (2000).

976 67. W. Li, S. H. DeVries, Separate blue and green cone networks in the mammalian retina. *Nature*
977 *neuroscience* **7**, 751-756 (2004).

978 68. H. Kolb, P. Goede, S. Roberts, R. McDermott, P. Gouras, Uniqueness of the S-cone pedicle in
979 the human retina and consequences for color processing. *J.Comp.Neurol.* **386**, 443-460 (1997).

980 69. Y. Tsukamoto, P. Masarachia, S. J. Schein, P. Sterling, Gap junctions between the pedicles of
981 macaque foveal cones. *Vision Res.* **32**, 1809-1815 (1992).

982 70. H. Hofer, J. Carroll, J. Neitz, M. Neitz, D. Williams, Organization of the human trichromatic cone
983 mosaic. *J Neurosci* **25**, 9669-9679 (2005).

984 71. W. B. Thoreson, S. C. Mangel, Lateral interactions in the outer retina. *Progress in retinal and*
985 *eye research* **31**, 407-441 (2012).

986 72. J. D. Crook, M. B. Manookin, O. S. Packer, D. M. Dacey, Horizontal cell feedback without cone
987 type-selective inhibition mediates "red-green" color opponency in midget ganglion cells of the
988 primate retina. *J Neurosci* **31**, 1762-1772 (2011).

989 73. L. E. Wool *et al.*, Nonselective Wiring Accounts for Red-Green Opponency in Midget Ganglion
990 Cells of the Primate Retina. *J Neurosci* **38**, 1520-1540 (2018).

991 74. P. R. Martin, E. M. Blessing, P. Buzas, B. A. Szmajda, J. D. Forte, Transmission of colour and
992 acuity signals by parvocellular cells in marmoset monkeys. *J Physiol* **589**, 2795-2812 (2011).

993 75. A. K. Goodchild, T. L. Chan, U. Grünert, Horizontal cell connections with short-wavelength-
994 sensitive cones in macaque monkey retina. *Vis. Neurosci.* **13**, 833-845 (1996).

995 76. D. M. Dacey, B. B. Lee, D. K. Stafford, J. Pokorny, V. C. Smith, Horizontal cells of the primate
996 retina: cone specificity without spectral opponency. *Science* **271**, 656-659 (1996).

997 77. T. L. Chan, U. Grünert, Horizontal cell connections with short wavelength-sensitive cones in the
998 retina: A comparison between New World and Old World primates. *J.Comp.Neurol.* **393**, 196-
999 209 (1998).

1000 78. Y. Tsukamoto, N. Omi, Some OFF bipolar cell types make contact with both rods and cones in
1001 macaque and mouse retinas. *Frontiers in neuroanatomy* **8**, 105 (2014).

1002 79. Y. Tsukamoto, N. Omi, OFF bipolar cells in macaque retina: type-specific connectivity in the
1003 outer and inner synaptic layers. *Frontiers in neuroanatomy* **9**, 122 (2015).

1004 80. L. Della Santina *et al.*, Glutamatergic Monopolar Interneurons Provide a Novel Pathway of
1005 Excitation in the Mouse Retina. *Current biology : CB* **26**, 2070-2077 (2016).

1006 81. S. C. Lee, F. Weltzien, M. C. Madigan, P. R. Martin, U. Grünert, Identification of AII amacrine,
1007 displaced amacrine, and bistratified ganglion cell types in human retina with antibodies against
1008 calretinin. *J Comp Neurol* **524**, 39-53 (2016).

1009 82. J. B. Demb, J. H. Singer, Intrinsic properties and functional circuitry of the AII amacrine cell.
1010 *Visual neuroscience* **29**, 51-60 (2012).

1011 83. J. S. Diamond, Inhibitory Interneurons in the Retina: Types, Circuitry, and Function. *Annu Rev*
1012 *Vis Sci* **3**, 1-24 (2017).

1013 84. M. B. Manookin, D. L. Beaudoin, Z. R. Ernst, L. J. Flagel, J. B. Demb, Disinhibition combines
1014 with excitation to extend the operating range of the OFF visual pathway in daylight. *J Neurosci*
1015 **28**, 4136-4150 (2008).

1016 85. H. Wassle, C. Puller, F. Muller, S. Haverkamp, Cone contacts, mosaics, and territories of bipolar
1017 cells in the mouse retina. *J Neurosci* **29**, 106-117 (2009).

1018 86. D. M. Dacey, J. D. Crook, O. S. Packer, Distinct synaptic mechanisms create parallel S-ON and
1019 S-OFF color opponent pathways in the primate retina. *Visual neuroscience* **31**, 139-151 (2014).

1020 87. K. J. Miyagishima, U. Grünert, W. Li, Processing of S-cone signals in the inner plexiform layer of
1021 the mammalian retina. *Visual neuroscience* **31**, 153-163 (2014).

1022 88. C. S. Cowan *et al.*, Cell Types of the Human Retina and Its Organoids at Single-Cell Resolution.
1023 *Cell* **182**, 1623-1640 e1634 (2020).

1024 89. T. Puthussery, S. Venkataramani, J. Gayet-Primo, R. G. Smith, W. R. Taylor, NaV1.1 channels in
1025 axon initial segments of bipolar cells augment input to magnocellular visual pathways in the
1026 primate retina. *J Neurosci* **33**, 16045-16059 (2013).

1027 90. J. Li *et al.*, Comprehensive single-cell atlas of the mouse retina. *iScience* **27**, 109916 (2024).

1028 91. W. Yan *et al.*, Mouse Retinal Cell Atlas: Molecular Identification of over Sixty Amacrine Cell
1029 Types. *J Neurosci* **40**, 5177-5195 (2020).

1030 92. S. Riccitelli, A. L. Vlasits, K. Franke, Behavior-Specific Computations in the Vertebrate Retina.
1031 *Annu Rev Vis Sci* **11**, 149-173 (2025).

93. D. Kerschensteiner, Feature Detection by Retinal Ganglion Cells. *Annu Rev Vis Sci* **8**, 135-169 (2022).

94. J. C. Hsiang, N. Shen, F. Soto, D. Kerschensteiner, Distributed feature representations of natural stimuli across parallel retinal pathways. *Nature communications* **15**, 1920 (2024).

95. P. Lennie, J. A. Movshon, Coding of color and form in the geniculostriate visual pathway (invited review). *Journal of the Optical Society of America. A, Optics, image science, and vision* **22**, 2013-2033 (2005).

96. J. D. Crook, O. S. Packer, J. B. Troy, D. M. Dacey, "Synaptic mechanisms of color and luminance coding: rediscovering the X-Y dichotomy in primate retinal ganglion cells" in The New Visual Neurosciences*,* L. M. Chalupa, J. S. Werner, Eds. (MIT press, Cambridge, MA, 2014), chap. 11, pp. 123-144.

97. G. T. Prusky, R. M. Douglas, Characterization of mouse cortical spatial vision. *Vision Res* **44**, 3411-3418 (2004).

98. J. Y. Lettvin, H. R. Maturana, W. McCulloch, W. H. Pitts, What the frog's eye tells the frog's brain. *Proc IRE* **47**, 1940-1951 (1959).

99. M. Rucci, M. Poletti, Control and Functions of Fixational Eye Movements. *Annu Rev Vis Sci* **1**, 499-518 (2015).

100. H. K. Ko, M. Poletti, M. Rucci, Microsaccades precisely relocate gaze in a high visual acuity task. *Nature neuroscience* **13**, 1549-1553 (2010).

101. M. Poletti, M. Rucci, A compact field guide to the study of microsaccades: Challenges and functions. *Vision Res* **118**, 83-97 (2016).

102. S. K. Shevell, P. R. Martin, Color opponency: tutorial. *Journal of the Optical Society of America. A, Optics, image science, and vision* **34**, 1099-1108 (2017).

103. A. Stockman, D. H. Brainard, "Color Vision Mechanisms" in OSA Handbook of Optics*,* M. Bass, Ed. (McGraw-Hill, New York, 2010), pp. 11.11-11.104.

104. P. Lennie, P. W. Haake, D. R. Williams, "The design of chromatically opponent receptive fields" in Computational models of visual processing*,* M. S. Landy, J. A. Movshon, Eds. (The MIT Press, Cambridge MA, 1991), pp. 71-82.

105. G. D. Field *et al.*, Functional connectivity in the retina at the resolution of photoreceptors. *Nature* **467**, 673-677 (2010).

106. Y. J. Kim, O. Packer, D. M. Dacey, A circuit motif for color in the human foveal retina. *Proceedings of the National Academy of Sciences of the United States of America* **121**, e2405138121 (2024).

107. S. Popovych *et al.*, Petascale pipeline for precise alignment of images from serial section electron microscopy. *Nature communications* **15**, 289 (2024).

108. D. G. Lowe (1999) Object recognition from local scale-invariant features. in *Proceedings of the Seventh IEEE International Conference on Computer Vision* (IEEE, Kerkyra, Greece), pp 1150-1157.

109. S. Saalfeld, R. Fetter, A. Cardona, P. Tomancak, Elastic volume reconstruction from series of ultra-thin microscopy sections. *Nature methods* **9**, 717-720 (2012).

110. T. M. Consortium *et al.*, Functional connectomics spanning multiple areas of mouse visual cortex. *bioRxiv* 10.1101/2021.07.28.454025, 2021.2007.2028.454025 (2023).

111. K. Lee, J. Zung, P. H. Li, V. Jain, H. S. Seung, Superhuman accuracy on the SNEMI3D connectomics challenge. *arXiv* **preprint arXiv:1706.00120** (2017).

112. K. Lee, R. Lu, K. Luther, H. S. Seung, Learning and Segmenting Dense Voxel Embeddings for 3D Neuron Reconstruction. *IEEE Trans Med Imaging* **40**, 3801-3811 (2021).

113. T. Macrina *et al.*, Petascale neural circuit reconstruction: automated methods. *bioRxiv* 10.1101/2021.08.04.455162, 2021.2008.2004.455162 (2021).

114. S. Dorkenwald *et al.*, CAVE: Connectome Annotation Versioning Engine. *Nature methods* 10.1038/s41592-024-02426-z (2025).

115. J. Maitin-Shepard *et al.* (2021) google/neuroglancer.

116. B. B. Boycott, H. Wässle, Morphological classification of bipolar cells of the primate retina. *Eur.J.Neurosci.* **3**, 1069-1088 (1991).

117. H. Wässle, B. B. Boycott, Functional architecture of the mammalian retina. *Physiol.Rev.* **71**, 447-480 (1991).

118. N. L. Turner *et al.* (2020) Synaptic Partner Assignment Using Attentional Voxel Association Networks. in *IEEE 17th International Symposium on Biomedical Imaging (ISBI)*, pp 1-5.

119. R. Lu, A. Zlateski, H. S. Seung, Large-scale image segmentation based on distributed clustering algorithms. *arXiv* **arXiv.** http://arxiv.org/abs/2106.10795 **[cs.CV]**, 1-8 (2021).

120. G. S. Bryman, A. Liu, M. T. H. Do, Optimized Signal Flow through Photoreceptors Supports the High-Acuity Vision of Primates. *Neuron* **108**, 335-348 e337 (2020).

121. J. van Hateren, T. Lamb, The photocurrent response of human cones is fast and monophasic. *BMC neuroscience* **7**, 34 (2006).

122. T. D. Lamb, E. N. Pugh, Jr., A quantitative account of the activation steps involved in phototransduction in amphibian photoreceptors. *J Physiol* **449**, 719-758 (1992).

123. S. Nikonov, N. Engheta, E. N. Pugh, Jr., Kinetics of recovery of the dark-adapted salamander rod photoresponse. *The Journal of general physiology* **111**, 7-37 (1998).

124. P. D. Calvert, T. W. Ho, Y. M. LeFebvre, V. Y. Arshavsky, Onset of feedback reactions underlying vertebrate rod photoreceptor light adaptation. *The Journal of general physiology* **111**, 39-51 (1998).

125. R. Hamer, S. Nicholas, D. Tranchina, T. Lamb, J. Jarvinen, Toward a unified model of vertebrate rod phototransduction. *Visual neuroscience* **22**, 417-436 (2005).

126. J. H. van Hateren, A cellular and molecular model of response kinetics and adaptation in primate cones and horizontal cells. *J Vis* **5**, 331-347 (2005).

127. J. H. van Hateren, H. P. Snippe, Simulating human cones from mid-mesopic up to high-photopic luminances. *J. Vis.* **7 4**, 1-11 (2007).

128. D. A. Baylor, B. J. Nunn, J. L. Schnapf, Spectral sensitivity of cones of the monkey *Macaca fascicularis*. *J.Physiol.(Lond.)* **390**, 145-160 (1987).

129. H. J. Dartnall, J. K. Bowmaker, J. D. Mollon, Human visual pigments: microspectrophotometric results from the eyes of seven persons. *Proc R Soc Lond B Biol Sci* **220**, 115-130 (1983).

130. A. Stockman, L. T. Sharpe, C. Fach, The spectral sensitivity of the human short-wavelength sensitive cones derived from thresholds and color matches. *Vision Res.* **39**, 2901-2927 (1999).

131. M. Srinivas *et al.*, Functional properties of channels formed by the neuronal gap junction protein connexin36. *J Neurosci* **19**, 9848-9855 (1999).

132. B. Teubner *et al.*, Functional expression of the murine connexin 36 gene coding for a neuron-specific gap junctional protein. *J Membr Biol* **176**, 249-262 (2000).

1118 133. R. G. Smith, NeuronC: a computational language for investigating functional architecture of
1119 neural circuits. *J.Neurosci.Methods* **43**, 83-108 (1992).

1120